Title

Quantitative In-Situ TEM Studies of Small-Scale Plasticity in Irradiated and Unirradiated Metals

Permalink

https://escholarship.org/uc/item/91r1m1q5

Author

Chisholm, Claire

Publication Date

2015

Peer reviewed|Thesis/dissertation

Quantitative *In Situ* TEM Studies of Small-Scale Plasticity
in Irradiated and Unirradiated Metals

By

Claire Chisholm

A dissertation submitted in partial satisfaction of the

requirements for the degree of

Doctor of Philosophy

In

Engineering – Materials Science and Engineering

in the

Graduate Division

of the

University of California, Berkeley

Committee in charge:

Professor Andrew M. Minor, Chair
Professor John W. Morris, Jr.
Professor Peter Hosemann

Summer 2015

Abstract

Quantitative *In Situ* TEM Studies of Small-Scale Plasticity in Irradiated and Unirradiated Metals

By

Claire Chisholm

Doctor of Philosophy in Materials Science and Engineering

University of California, Berkeley

Professor Andrew M. Minor, Chair

In this work, unirradiated and irradiated model body centered cubic (BCC) and face centered cubic (FCC) materials are investigated using advanced electron microscopy techniques to quantitatively measure local stresses and strains around defects, with the overarching goal of obtaining a fundamental understanding of defect physics.

Quantitative in-situ transmission electron microscopy (TEM) tensile tests are performed with Molybdenum-alloy nano-fibers, functioning as a model BCC structural material. Local true stress and strain around an active Frank-Read type dislocation source are obtained using quantitative load-displacement data and digital image correlation. A mixed Frank-Read dislocation source, $b=a/2[-1-11](112)$ with a line direction 20° from a screw orientation and length 177 nm, is observed to begin operating at a measured local stress of 1.38 GPa. The measured local true stress values compare very well to estimated stresses using dislocation radius of curvature, and a line-tension model of a large bow-out configuration, with differences of only ~1%. The degree to which the local true stresses can be measured is highly promising. However, the ultimate failure mode of these fibers, sudden strain softening after dislocation starvation and exhaustion, cannot be captured at the typical camera frame rate of 30 frames per second. Thus, fibers are mechanically tested while under observation with the Gatan K2-IS direct electron detector camera, where the frame rate is an order of magnitude larger at 400 fps. Though the increase in frame rate adds to the overall understanding of the sudden failure, by definitively showing that the nano-fibers break rather than strain soften, the failure mechanism still operates too quickly to be observed. In the final investigation of this BCC model structural alloy, the mechanical behavior of heavily dislocated, but unirradiated, and He^{1+} and Ni^{2+} irradiated nano-fibers are compared. Remarkable similarities are found in the mechanical data, as the two defect conditions exhibit similar yield strengths, ultimate tensile strengths, and number and size of load-drops. This similarity implies that, even if materials contain dissimilar individual defects, the collective defect behavior can result in similar mechanical properties. Thus, the origin of mechanical properties can be ambiguous and caution should be taken when extrapolating to different size scales. Furthermore, such similarities highlight the importance of in-situ observation during deformation. These experiments provide a key test of theory, by providing a *local* test of behavior, which is much more stringent than testing behaviors averaged over many regions.

Advanced electron microscopy imaging techniques and quantitative in-situ TEM tensile tests are performed with Au thin-film as a model FCC structural material. These investigations highlight the various hurdles experimental studies must overcome in order to probe defect behavior at a fundamental level. Two novelly-applied strain mapping techniques are performed to directly measure the matrix strain around helium bubbles in He^{1+} implanted Au thin-film. Dark-field inline holography (DFIH) is applied here for the first time to a metal, and nano-beam electron diffraction (NBED) transient strain mapping is shown to be experimentally feasible using the high frame rate Gatan K2 camera. The K2 camera reduces scan times from ~18 minutes to 82 seconds for a 128x256 pixel scan at 400 fps. Both methods measure a peak strain around 10 nm bubbles of 0.7%, correlating to an internal pressure of 580 MPa, or a vacancy to helium ion ratio of 1V:2.4He. Previous studies have relied on determining the appropriate equation of state to relate measured or approximated helium density to internal bubble pressure and thus strain. Direct measurement of the surrounding matrix strain through DFIH and NBED methods effectively bypasses this step, allowing for easier defect interaction modeling as the bubble can be effectively simplified to its matrix strain. Furthermore, this study demonstrates the feasibility of fully strain mapping, in four dimensions, any in-situ TEM experiment. The final set of experiments with this model FCC structural material shows the attempted correlation of defect interactions and deformation behavior at the nano-scale. Experimental comparison of mechanical behavior from quantitative in-situ TEM tensile tests of focused ion beam (FIB) shaped, He^{1+} implanted, and FIB-shaped He^{1+} implanted Au thin-film show a wide range of behavior that could not be directly linked to irradiation condition. This is due to the large role that overall microstructural features, such as grain boundary orientation and texture, play in mechanical behavior at this size scale. However, these tests are some of the first to in-situ TEM mechanically strain single grain-boundaries free of FIB-damage. It is expected that, with well-defined grain orientations and boundaries, real conclusions can be made.

For my father, Matt, who piqued my interests

For my mother, Kathy, who nurtured them

For my siblings, Erica, Sarah, and Michael, who all got to go to "bring your kid to work" day except me

For my partner, Erich, whose love, support, and encouragement has brought me to this end

Table of Contents

Acknowledgements

1. Introduction and Background

1.1 Motivation

The field of materials science is striving toward a more complete understanding of materials. Ideally, we would like to use our knowledge to start with individual atoms and eventually form whole rocket engines, nuclear reactors, etc., then predict material behavior and evolution over the lifetime of the modeled construct. Achieving a greater understanding of the underlying physics of defects and their role in materials behavior is part of the knowledge base we would like to build. As a stepping-stone, experiments that probe the fundamental deformation of materials must be used to shape computational simulations of plastic behavior in materials. Of particular interest, and explored in this work, are the interaction of defects and the mechanical response of metals. Though inherent physical limitations exist, experiments are approaching the spatial and temporal regimes of computational simulations as electron microscopes and other probes improve.

The first recorded experiment to approach the mechanical testing of single defects came from Leonardo da Vinci[1]. Da Vinci outlines in his notebooks an experiment measuring the tensile strength of iron wire with ever decreasing lengths, finding shorter wires carried higher load. Classical understanding of the mechanics of materials maintains there should be no difference in tensile strength as sample length changes, and as such, the results were later assumed to arise from errors in translation and recording[2]. 450 years after da Vinci, S.S. Brenner confirmed the seemingly erroneous results by demonstrating shorter, single-crystalline whiskers of several metals are indeed stronger than their longer counterparts[3]. And in one of the first modern experiment of its kind, M.D. Uchic and coauthors performed quantitative in-situ scanning electron microscope (SEM) compression tests of bulk materials, machined to the micron scale with a focused ion beam (FIB)[4]. Not only are the SEM compression results in line with the previous "shorter is stronger" findings, their sample-preparation method demonstrated the possibility for similar investigations into almost any inorganic material. Attributing these results, spanning from c.1500 to now, to a decreased presence and likelihood of weak defects, leads to the premise that mechanical properties of bulk materials are averages of their individual defect strengths. Thus, the challenge becomes observing and isolating individual defects and measuring their interactions. This work is an investigation of how to experimentally quantify the stresses and strains associated with individual defects in metals, striving toward the exploration of fundamental materials behavior.

1.2 Deformation of metals

From the extensive breadth of materials and defects, this study focuses on two metals, a molybdenum-alloy with body centered cubic (BCC) crystal structure, and gold with face centered cubic (FCC) crystal structure. Further focus-refinement is made by limiting observations to dislocations and common irradiation-induced defects.

1.2.1 Dislocations

Dislocations were predicted as the primary means of carrying plasticity in crystalline materials in 1934[5–10], decades before they were first directly observed in metals in 1956[11].

Indeed many of the equations describing their production, motion, and interaction, though elegant, were developed before they were observed and are still being refined, largely through computational means.

Dislocations are driven to straighten in order to minimize energy. As they move under a resolved shear stress in the glide plane, τ, and become pinned, a force, τb acts normal to the dislocation line to move the dislocation, b, forward, bowing it. The dislocation "line tension", T, acts to return the dislocation to the straight, shortest distance path between pins. The line tension can then be thought of as the change in configurational, or self, energy of the dislocation as the length of the dislocation changes, or

$$T = \frac{\partial W(\theta)}{\partial L(\theta)},$$
(1.2.1)

where θ is a term that describes the dislocation configuration. If the following assumptions are made: the volume is isotropic, other interactions of the new configuration can be neglected, and the self-energy per length of the curved dislocation is the same as the self-energy per length of the original straight dislocation, the line tension can be approximated as

$$T = \mu b^2,$$
(1.2.2)

where μ is the shear modulus of the material, and b is the Burgers vector. Much has been done with dislocation theory to eliminate these assumptions[12]; however, the many details are beyond the scope of the present study. Thus, by examining a section of the dislocation, dL, balancing the driving force with the line tension, as shown in Figure 1.2.1, and using the small-angle approximation, the resolved shear stress can be estimated from the radius of curvature of the dislocation as

$$\tau(R) \approx \frac{\mu b}{R}$$
(1.2.3)
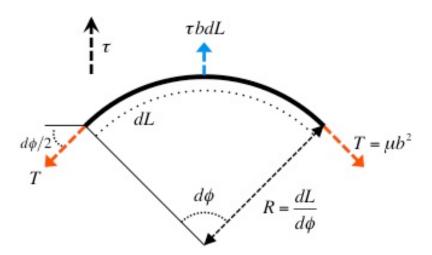
Figure 1.2.1: Exaggerated schematic showing the force balance on a dislocation segment acted on by the resolved shear stress, τ.

There are many possible dislocation multiplication mechanisms; considered one of the most important, is the Frank-Read (F-R) source. In this mechanism a dislocation is pinned between two nodes, and the dislocation line bows out as the resolved shear stress increases. Past a critical point, generally when the radius of curvature of the dislocation is equal to half the distance between the pinning nodes, or half the source length, the dislocation will spiral around the pinning points until the two sides, of opposite line direction, annihilate, creating a loop that will expand while leaving behind a dislocation between the two nodes. This process can then repeat. At this point the anisotropy of the material will play a role. For example, dislocation dynamics simulations[13] have shown an increase in anisotropy will decrease the critical stress to activate the mechanism. Most BCC metals have anisotropy coefficients

$$A = \frac{2c_{44}}{c_{11} - c_{12}},$$ (1.2.4)

where c_{ij} are the first-order elastic constants, that are larger than the isotropic value of one. Notable exceptions are molybdenum and niobium, whose anisotropy coefficients are less than one. Figure 1.2.2 shows representative F-R source configurations for initial dislocations with edge, screw, and mixed character in a BCC material. For isotropic materials, the generated loops are generally circular in FCC materials, and elliptical in BCC materials. This is due to the often larger stress required to move a dislocation beyond one Burgers vector, called the Peierls-Nabarro stress (PNS), when it has screw character. Anisotropy can also change the shape of the generated dislocation, as it affords the lower-energy segments the opportunity to straighten, as in Figure 1.2.2a,b.
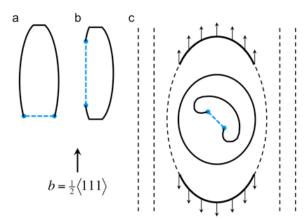
Figure 1.2.2: Schematics of the F-R source in a BCC material with three different initial dislocation configurations with b=1/2<111> (blue dashed line). (a-b) These show the effect of increased anisotropy on the dislocation shape, shown just before the activation stress. After [13]. (a) Edge: The edge portion of the dislocation can easily glide by extending along the screw segments. (b) Screw: The dislocation must generate edge portions and does not extend as far. (c) Mixed: This schematic assumes isotropy and shows the source after 4 operations, with a 5th in progress. The larger screw PNS results in elliptical loops with mixed portions (solid black lines) that can easily glide, leaving a local dislocation structure of loops confined by slower-moving nominally-screw dislocation pairs (black dashed lines). After [14].

To generalize the F-R source activation stress to include the actual dislocation configuration, a geometrical constant, α, is added to the force balance of eq. 1.2.3. Thus, the activation stress of a F-R source, as a function of the source length, L, is

$$\tau(L) = \frac{\alpha\mu b}{L} , \qquad (1.2.5)$$

where $\alpha \approx 1$.

If we now consider external forces acting on the dislocation, the stress to bow a dislocation to the critical point becomes

$$\tau_{CRSS}(L) = \frac{\alpha\mu b}{L} + \tau_{ex} + \tau_O \qquad (1.2.6)$$

where τ_{ex} is the stress required to overcome external forces, such as other dislocations or image forces, and τ_o is the lattice friction stress, or PNS.

The stress to activate a F-R source is investigated in §2.3.1, by comparing local quantitative stress measurements with the radius-of-curvature method using equation 1.2.3, and predicted activation stress as a function of source length using equation 1.2.6. High temporal-resolution experiments, presented in §2.3.2, investigate the possible dislocation multiplication mechanisms at play at the high stresses often reached in nano-scale mechanical testing.

1.2.2 Irradiation defects

Ion irradiation has been used experimentally to simulate the displacement damage of materials under neutron irradiation for many decades[15–17] The process is much faster, taking hours to accumulate displacement damage that would take years under reactor conditions, and the irradiated material usually remains inactive, as ion irradiation rarely leads to fission. This leaves the sample more easily and safely investigated. By adding helium implantation to simulate the production of alpha particles, a common decay product, the damage accumulation can more closely approximate reactor conditions.

One problem facing materials under high-temperature reactor conditions is swelling. This is a result of helium or other gaseous fission products, which are insoluble in most materials, accumulating with vacancies to form rapidly growing voids. Voids are 3-dimensinoal clusters of gas ions and vacancies with little or no internal pressurization, and are in equilibrium with the surrounding matrix, often resulting in faceted boundaries that correspond to the close-packed plane of the matrix material. Voids grow from bubbles, which are pressurized cavities of gas ions and vacancies, and usually spherical in shape. The bubbles grow, acting as sinks for vacancies and gas ions, until they reach a critical radius and then begin to grow exponentially as voids. Many of the techniques used to mitigate swelling focus on maintaining bubble radii below the critical size, often by creating gas ion and vacancy sinks. One ever-present sink in bulk materials are its grain boundaries. This affords a heterogeneous nucleation site for bubbles, with the consequence of embrittling the grain boundary[18,19]. At present, experimental observations of the transition from bubble to void are lacking, though this transition is important for understanding swelling behavior[19,20].

Common defect accumulations in irradiated metals are stacking fault tetrahedra (SFT) and small vacancy or interstitial defect clusters, often referred to as simply "black spot damage", after their appearance in diffraction-contrast transmission electron microscopy (TEM). These clusters usually act as impedance to dislocation motion, eventually shearing if they are low strength and pinning the dislocation, as in Orowan strengthening, at higher strengths, and in general lower the ductility of the material, but can also grow, agglomerate, or glide, participating in the overall plasticity[21–27].

The strains around He^{1+} cavities in a thin film are mapped by two methods to show the feasibility of 4-D strain mapping of the bubble-to-void transformation in §3.3.1. The mechanical properties and deformation mechanisms of unirradiated thin-film are compared to three irradiation cases in §3.3.2, and examine the ductility of single grain-boundaries. The mechanical properties and deformation mechanisms of an ion irradiated and He^{1+} implanted nano-fiber are presented in §2.3.3, and compared to an unirradiated nano-fiber with similar initial dislocation density.

1.3 Small-scale mechanical testing

The American Society for Testing and Materials (ASTM), International Organization for Standardization (ISO), and European Norm (EN) standard procedures for mechanical testing of bulk metals are uniaxial tensile testing or plane strain conditions in the case of high strain rate fracture testing. The advantages of uniaxial tensile testing over compression or indentation include: a nominally uniform stress and strain state, which allows for straightforward interpretation of data, and fewer sample-limiting constraints, including aspect ratio or cross-sectional shape, that can lead to elastic instabilities in compression in the form of buckling or stress concentrations in non-circular shaped cross-sections. And by maintaining a plane strain condition, thin-film effects can be avoided. Thus, the challenges faced in small-scale mechanical testing include tensile sample preparation that isolates individual defect structures with dimensions that ensure a plane strain condition, stable and refined tensile actuation, and quantitative, high-resolution measurement of local strain and stress.

1.3.1 Sample preparation

For direct observation of individual defect interactions, the TEM is an obvious choice of platform. However, this necessitates electron transparent samples. Traditionally, the materials available to nano-scale mechanical experiments were limited to those that could be grown as thin-films or fibers. The development of the FIB as a sample preparation tool widened availability to nearly any inorganic material, with the added flexibility of site-specificity, such as locating a precise crystal orientation or a grain boundary. However, there are major drawbacks, including sample surface damage and ion implantation, both of which have been shown to affect material deformation mechanisms. For example, this damage can manifest as the failure site of pristine nano-fibers[28], or cause grain boundary embrittlement in the case of aluminum and Ga$^+$ ions, used in most FIB microscopes[29,30]. There are many papers[31,32] and review articles[33–35] highlighting the advantages, drawbacks, and damage mitigation techniques[36–39] of the FIB as a sample preparation tool, and is further explored in §3.3.2.

1.3.2 Actuation

TEM-based actuation is a unique challenge. The TEM holder must meet vacuum specifications, operate in the limited space afforded by the pole piece gap of the TEM, and be stable enough to produce high quality observations. There are many reviews[40,41], updated periodically as technology improves, and this section merely outlines common solutions to the unique requirements of individual experiments. The first commercially available version of straining holders was mechanical, using gearboxes and electrical motors for actuation[42]. They are largely robust, achieving displacement rate control from the microns down to the tens of nanometers per second. Piezoelectric-based actuation has a displacement resolution that is largely limited by the electronics, and their associated noise, used to control them, as any change in electric field will generate a mechanical response of the piezoelectric. They afford flexibility in testing when used in a stack, which allows for fully 3-D displacement control. With the advancement of bulk and surface micromachining, the selective etching or building of silicon-based materials into micro electro mechanical systems (MEMS) devices has resulted in the ability of many research groups to fabricate their own designs for stand-alone devices based on thermomechanical[43] or electrostatic[44] actuation.

1.3.3 Strain measurement and mapping

There are two overarching methods to measure sample strain during in-situ experiments: imaging based-methods and directly through the actuator. The development and application of in-situ TEM CCD and other technology-based cameras, along with the increase in processing speed and data storage, has opened the options of imaged-based strain measurement and mapping considerably. Electron microscopy-based methods include high-resolution convergent beam electron microscopy (CBED), nano-beam electron diffraction (NBED), and many types of holography. The advantages and drawbacks of some of these methods can be found elsewhere[45–47], and, as of yet, are not widely used during in-situ TEM mechanical testing. Experimental hurdles that must be overcome include reducing the effect of mechanical vibration and drift, data storage, and the ability to simultaneously measure or map strain while visualizing the sample. Digital image correlation (DIC), when applied to in-situ TEM acquired video, has been successfully applied to in-situ TEM mechanical testing[40,48,49]. One difficulty in applying DIC to TEM images is the reliance on unchanging features, which can be difficult to achieve in diffract-contrast imaging. With appropriately trackable features the method can achieve sub-pixel displacement resolution[50,51]. Actuation-based strain measurement, for example in electrostatic actuators, piezo-electric actuators, and MEMS devices that use resistive heating, the displacement is a function of the input voltage. These methods have displacement resolutions that are as high as their electrical noise and sensitivities allow.

1.3.4 Stress measurement

Stress measurement during in-situ TEM mechanical experiments likewise has two primary methods, image and device-measured. An example of image-based local stress measurement relates the dislocation radius of curvature to the stress required to achieve the shape through the line tension model, with the obvious downside being the reliance on the presence of dislocations that can be characterized. This method has been discussed in depth

elsewhere[12], and is further investigated in §2.3.1. An example of device-measured load comes from electrostatically actuated nano-indenters, which measure applied force through a change in distance between two capacitive plates[52,53], one of which is attached to the actuated crosshead, and the other is fixed.

1.4 Size effect

The original premise of this work postulates that no inherent difference in mechanical behavior or properties as sample size decreases past the micron limit. The increased strength can be accounted for by the stochastics of the limitation of size and number of defects that approach pristine conditions, rather than a change in underlying physics[54]. Indeed, any intrinsic size effect implies mechanical testing at this size scale cannot directly measure the fundamental physical phenomena, and as such, properties cannot be extrapolated to the bulk without a thorough understanding of the intrinsic effects on behavior as sample size decrease. Size dependence of material properties is seen as the surface to volume ratio increases, for example increased Young's modulus in Si nano-wires smaller than 100 nm[55,56], and increased flow stress in FIB-shaped pillars[57]. However, surface effects can be circumvented with large enough samples, and the size-effect in FIB-machined samples has been shown[31,37,38] to be a direct result of the FIB-damage, which can be avoided by forgoing FIB-machining. Measurements of local stress around a dislocation source, presented in §2.3.1, show by direct comparison to continuum-based models, whether any inherent size effect exists, and whether direct correlation to the bulk can be made. There are several comprehensive studies and reviews dedicated to the state of current understanding of the material size effect[58–60]. One notable study, by J.A. El-Awady, seeks to establish a constitutive model that would allow extrapolation of nano-scale dislocation mechanisms to the bulk[61]. While the results are extremely thorough and useful, a constitutive model falls short of the goal of true understanding and may lack applicability to advanced materials, such as gum metal[62,63].

Chapter 2: BCC Molybdenum Alloy Nano-Fibers

Refractory metals, such as Mo, are current candidates for use in advanced fission and fusion reactor designs due to their high melting points and high strengths even at increased temperatures, natural resistance to radiation-induced swelling, and resistance to corrosion by liquid metal coolants. However, there are still problems with radiation induced property degradation to address, such as the low-temperature radiation-induced increase of the ductile to brittle transition temperature, or high-temperature helium embrittlement[64]. Single crystalline Mo-alloy nanofibers are ideal specimens to use when studying the defect interactions in BCC materials that are still not fully understood. This is due to the ease of which uniaxial tensile samples can be prepared without the deleterious effects of focused ion beam milling (§1.3.1), with sizes that can range from 300 to 1600 nm by varying growth parameters (§2.1.1), and with tailorable initial dislocation densities (§2.1.2).

2.1 Sample preparation of Mo-alloy nano-fibers

2.1.1 Directional solidification of ternary eutectic alloy

Mo-alloy (Mo-10Al-4Ni at.%) nanofibers were prepared by arc melting and directional solidification of a Ni-45.5Al-9Mo (at.%) eutectic composite. The Mo, Al, and Ni, all >99.99% pure, were weighed then mixed using arc melting and drop cast. The drop cast ingot was then directionally solidified in flowing argon gas using an optical floating zone furnace. Using a fast, but stable, growth rate of 80mm/h single crystal Mo-alloy nanofibers, with approximately square cross-sections and edge lengths of ~200 nm, were grown with the fiber axes along the <001> direction. The edges of the fiber have a {110} orientation, though the corners were often truncated or rounded, resulting in an octagonal shape with 4 {110} and 4 {100} faces. Faster growth rates resulted in smaller, but defected fibers, often with kinks, branches, and uneven cross-sections, as seen in Figure 2.1.1. Fibers were revealed from the composite surface by selectively etching the Ni-Al matrix with an 18 vol.% HCl + 8 vol.% H_2O_2 + distilled/deionized (DI) water mixture for 2 minutes. The etching time was chosen to reveal at least 20 μm lengths of Mo-alloy fibers, which were then rinsed in deionized water and ultrasonicated in methanol to remove any residue from the etching process. A detailed description of the nanofibers synthesis procedure and characterization has been reported previously [54,65,66].

There is some evidence of small Al-rich FCC precipitates in the Mo-alloy nanofibers, detected by Selected Area Electron Diffraction (SAED) and atom-probe tomography [67]. However, after careful examination of similar long-exposure SAED patterns of the fibers mechanically tested here, no such precipitates were found. This may be due to inconsistencies in fabrication batches or the fibers themselves, imaging over a larger thickness (the fibers presented here were not thinned before examination), or some effect from the FIB machining Oveisi, et. al. used.
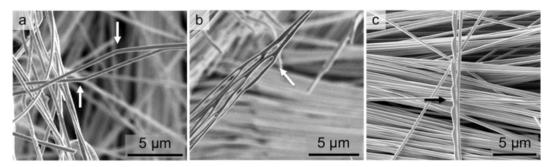
Figure 2.1.1: SEM micrograph of common microstructural defects in zone-solidified Mo-alloy nanofibers. (a) White arrows indicate kinks in the fiber, (b) white arrow indicates fiber with many branches, and (c) black arrow indicates a fiber with uneven cross-section.

2.1.2 Tailoring dislocation density

Introduction of defects into the nanofibers was achieved in two ways, pre-straining and irradiation. Varying degrees of dislocation density in the nanofibers can be achieved by pre-straining the NiAl-Mo composite after directional solidification. The composite was cut for a starting aspect ratio of 5:1 (10mm disk diameter with a 2mm thickness) and each end mechanically polished. The disk was then compressed parallel to the growth direction of the fibers at room temperature to a range of 0-15% engineering strain. 0% pre-strained fibers, or as-grown, were found to be nominally dislocation free, as seen in Figure 2.1.2a. 15% pre-strained fibers were found to have a fairly even distribution of dislocations throughout, with dislocation densities around 1.6×10^{14} m^{-2}, as seen in Figure 2.1.2c. Intermediate pre-straining resulted in heterogeneous packets of dislocations throughout as well as some dislocation debris in the form of small loops, as seen in Figure 2.1.2b, for dislocation densities between 1×10^{12} to 5×10^{13} m^{-2}.
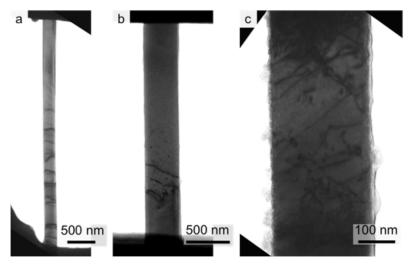
Figure 2.1.2: TEM micrographs of Mo-alloy nanofibers. (a) 0% pre-strained fiber showing no dislocations throughout the gage section. The black lines seen in the fiber are bend contours. (b) 9% pre-strained fiber showing 4 dislocations with some additional small dislocation debris loops, confined to one end of the sample. (c) 15% pre-strained fiber showing many dislocations all throughout the fiber. Also seen is residue from the etching process that was not adequately removed with the methanol wash.

2.1.3 Characterization of dislocations in pre-strained Mo-alloy fibers

To measure the dislocation density of the nanofibers, a square grid was overlaid on a projected TEM image of the fibers and the number of intersections of dislocation and grid were counted. The dislocation density was calculated based on Ham's method[68] as:

$$\rho_\perp = \frac{2NA_p}{V \cdot L}$$

(2.1.1)

where N is the total number of intersections, A_p is the projected area, V is the total volume of the portion of the fiber being analyzed, and L is the total length of grid lines used in analysis. A detailed investigation of the dislocation density of the fibers as a function of pre-strain can be found elsewhere[66].

Crystallographic analysis (g•b) of the dislocations in the intermediately pre-strained fibers indicate that the dislocations have a Burger's vector of type b = ½ <111>{112}. Due to experimental limitations, these analyses were done with only one axis of rotation, about the <001> growth direction of the fiber, thus the character (edge or screw) of the dislocation could not be uniquely determined without making assumptions based on the crystallographic geometry of the sample (§2.3.1). However, a recent study[69] of pre-strained Mo-alloy nanofibers using TEM analysis and tomography shows the long, straight dislocations have screw character, and the small dislocation debris is primarily b=½<111> prismatic loops.

2.1.4 In-situ ion irradiation and implantation of Mo-alloy fibers

Irradiation defects were introduced at room temperature through in-situ TEM ion irradiation and implantation. The In-situ Ion Irradiation TEM (I³TEM) at the Ion Beam Laboratory at Sandia National Laboratories was used for concurrent heavy and light ion irradiation and implantation. A review of this unique facility can be found elsewhere [70]. 9% pre-strained fibers that were fully etched away from the NiAl matrix were gathered onto a normal Cu TEM grid. Both 2.8 MeV Ni^{2+} and 10 keV He^{1+} ion beams were concurrently introduced into the heavily modified JEOL 2100 TEM along the same beam path, nominally orthogonal to the electron beam and at a 30° angle to the Cu Grid, as seen in the schematic of Figure 2.1.3. The irradiation experiments were performed at room temperature with the TEM operating at 200 keV, which is well below the knock-on threshold of molybdenum.
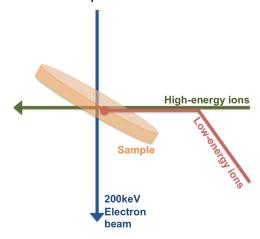
Figure 2.1.3: Graphical representation of I³TEM experimental setup.

Helium ions were chosen to mimic the alpha particle production that would be seen in neutron irradiation and the nickel ion species was chosen to simulate the displacement damage under neutron irradiation, as well as for chemical compatibility, as the nanofiber is already 4 at.% Ni. Chemical compatibility ensures no intermetallic compounds are created if the ion stops in the sample.

Dose rate, or ion flux, is calculated as

$$\dot{\Phi} = \frac{I}{A} \times \frac{6.241x10^{18} e/C}{Z_s} \tag{2.1.2}$$

where I is the current of the ion species, as measured with a suppressed Faraday cup before the sample, A is the beam spot size, as measured with a beam burn, and Z_s is the charge of the ion species. Beam burns are a method to measure beam spot size where a piece of tape is put on the end of a TEM holder and exposed to the ions beams, which burn the tape, as seen in Figure 2.1.4. Area of the beam burn is measured using the image processing and analysis program ImageJ. Ion flux is now measured directly at the I^3TEM with a custom Faraday stage.
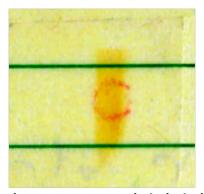
Figure 2.1.4: Photo of ion beam burn on tape. Red circle indicates where a 3 mm TEM disk would be. The tape is affixed to green-lined paper in this image.

10 keV He^{1+} was implanted at a dose rate of $3.2x10^{12}$ ions cm^{-2} s^{-1} to a dose of $3.0x10^{16}$ ions cm^{-2}. The fibers were concurrently irradiated with a 2.8 MeV Ni^{2+} ion beam at a dose rate of $1.1x10^{11}$ ions cm^{-2} s^{-1} to a dose of $1.0x10^{15}$ ions cm^{-2}. The damage-thickness profiles per ion, Figure 2.1.5, and sputter at both entry and exit surfaces were calculated for both ion species using the Transport of Ions in Matter (TRIM) monolayer calculation with a 0° incident angle and a layer thickness of 300nm [71]. An incident angle of 0° rather than 30° was used as the fibers were randomly distributed on the Cu TEM grid. The number of sputtered atoms was found to be negligible by SRIM simulation, and was therefore assumed to play no role in the experimental observations.

Displacement damage is shown as the number of displacements per atom, or dpa. It is the average number of times a target atom has moved, and is calculated as

$$dpa(t) = \frac{\Phi_s \times N_V(t)}{\rho_t} \tag{2.1.3}$$

where Φ_s is the dose, or ion fluence, N_V is the total vacancies created at each point of depth t, as calculated with the SRIM program, and ρ_t is the target density. This results in a calculated

maximum 5.5 dpa at 24 nm and an average 2.5 dpa for helium and nickel, respectively. The actual dose may vary per fiber due to variation of beam intensity or shadowing from other fibers, though care was taken when choosing a sample to take from fibers that were unlikely to have been shadowed.

Based on similar irradiation experiments and simulations performed by other groups, the irradiation damage is likely to be predominantly interstitial and vacancy dislocation loops of type b=½ <111> {110} and small defect clusters [72–78]. During and immediately after room temperature irradiation of the Mo-alloy nanofibers, no irradiation defects were observed. At room temperature, molybdenum is in Recovery Stage II, where interstitial point defects and clusters are mobile [79]. As seen in Figure 2.1.6b, after ten months of room temperature annealing, there is sufficient defect coalescence such that the final dislocation structure consists of irregularly shaped loops, dislocation segments, and small defect clusters. It should be noted that, even with a large He^{1+} dose, no helium cavities were found. Detailed characterization of dislocations was not performed on these irradiated Mo-alloy fibers as the thickness restricted optimal TEM conditions. Defect cluster density was found for several fibers to be between $2x10^{16}$ and $3x10^{22} cm^{-3}$, according to the method outlined by Jenkins [80]. This is lower than similar experiments, however it has been shown that substitutional impurities, like nickel and aluminum in these fibers, decrease the defect number and size [76]. There is also the possibility that the concentration of helium near the incident surface will result in a sort of layered structure. However, tilting of the irradiated fibers in the TEM shows no difference in defect density along the fiber thickness, and it is possible the helium escaped to the surface during the anneal, or diffused evenly throughout the fiber thickness.
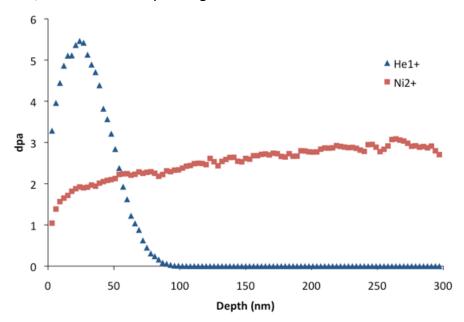
Figure 2.1.5: Depth-damage profile of 10 keV He^{1+} implantation and 2.8 MeV Ni^{2+} irradiation of Mo.
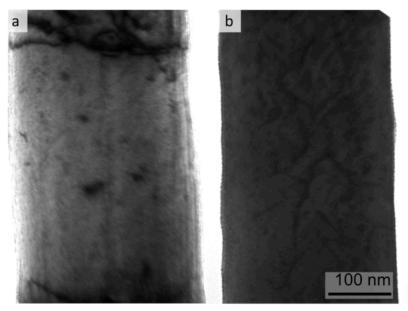
Figure 2.1.6: TEM bright-field micrographs of Mo-alloy nanofibers (a) before 10 keV He[1+] and 2.8 MeV Ni^{2+} irradiation, and (b) a different fiber after irradiation and 10 month room temperature anneal.

2.2 Experimental methods

2.2.1 Hysitron, Inc. PI-95 picoindenter

In-situ TEM tensile testing of the Mo-alloy nanofibers was conducted with a JEOL 3010 TEM operated at 300keV. A Hysitron, Inc. PI-95 Picoindenter was used in displacement-controlled indentation mode, with loading rates of usually 2 nm/s, and a doped-diamond 20 μm flat-punch indenter. The PI-95 simultaneously acquires quantitative raw load and displacement data. The device uses electrostatic actuation and capacitive plates for displacement sensing, resulting in an impressive quoted sub-nanometer displacement noise floor and sub 200 nN force noise floor. However, the experimental setup at the National Center for Electron Microscopy (NCEM), where the tensile testing was performed, introduces some external noise that results in load noise on the order of half a μN and displacement noise on the order of a nanometer (or, on average, ~16 MPa and 1.4×10^{-4} nm/nm).

2.2.2 Hysitron push-to-pull device

The compressive motion of the flat-punch picoindenter was converted to tensile strain in the Mo-alloy fibers via a MEMS fabricated push-to-pull (PTP) device. The PTP device is microfabricated on a silicon-on-insulator wafer and has a semicircular end where the flat-punch indenter contacts the device, as shown in Figure 2.2.1d. The PTP device has four identical springs distributed symmetrically at the corners so that a sample affixed across the middle gap of the PTP device is pulled in tension. The springs are designed to be stiffer in the lateral direction to ensure uniaxial tensile loading. By changing the dimensions of the springs, the inherent stiffness of the PTP device can be tuned to optimize sample protection during handling and the subsequent parameters of the test. The springs are arranged such that the force acting

on them is in parallel with the force on the tensile specimen. Stiffnesses used here ranged from 330 to 450 N/m. The PTP device is loaded in the PI-95 TEM holder by first affixing it to a small copper stub with the polymer adhesive Crystalbond. The copper stub is then screwed onto the end piece of the PI-95 TEM holder.

The fibers were transferred to the PTP device using an Omniprobe micromanipulator in a FEI Strata 235, a dual-beam Focused Ion Beam (FIB)/Scanning Electron Microscope (SEM) (Fig. Xa). Mo-alloy fibers were attached with electron beam induced deposition (EBID) of platinum (Pt) to the micromanipulator, and their other ends cut free from the bulk with a focused 30 keV gallium (Ga) ion beam at a current of 10 pA to yield fibers of lengths ranging from 10 to 60 μm. The fibers were then transferred to the PTP device, where both ends were attached with ~2x2x1 μm^3 grip pads, or "welds", of EBID-Pt (Figure 2.2.1b,c). Electron beam induced deposition of Pt was achieved with a 5 keV electron beam and methylcyclopentadienyl (trimethyl) platinum precursor material. To avoid ion beam damage to the fiber gage section during sample preparation, the fibers were cut using blind FIB cuts, meaning they were never imaged with the ion beam. This limits the exposure of the fiber to the ion beam to the cut points, which are well outside the gage sections.
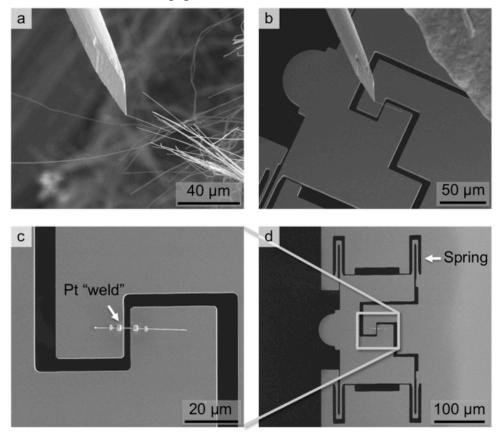
Figure 2.2.1: SEM micrographs of tensile sample making procedure. (a) Mo-alloy nanofibers are picked up with a micromanipulator, and (b) transported to the PTP device. Shown are the PTP device, the micromanipulator with attached fiber, and the Pt gas injection system in the upper right corner. (c) Mounted fiber with Pt "welds" or "grip pads". (d) Overall image of the PTP device. Indenter approaches the semicircular feature from the left.

2.2.3 Quantitative analysis of engineering stress and strain

To calculate the engineering stress on the nano-fiber, its initial cross-sectional area and the force applied were determined. The initial cross-sectional area of the fibers is assumed to be octagonal, as SEM images show this geometry is favored by the fibers (Figure 2.2.2a). To measure the initial cross-sectional area, the nanofibers were first tilted about their longitudinal axes, <001>, in the TEM to a zone-axis (ZA) condition. For example, when tilted to the <110> ZA, the fiber edge is orthogonal to the electron beam and the projected width is considered equal to the fiber edge width (Figure 2.2.2b). If tilted to ZA = <100> the projected width is equal to the diagonal of the cross section minus two identical right isosceles triangles. At least four projected widths, usually at ZA= <110>, <100>, <210>, and <310> and both clockwise and counter-clockwise of the <110> ZA, were acquired to obtain a full idea of the actual cross-sectional shape. However, it was found that each nano-fiber tested here is symmetric such that measuring just the <110> and <100> projected widths fully defines the fiber cross-sectional shape.
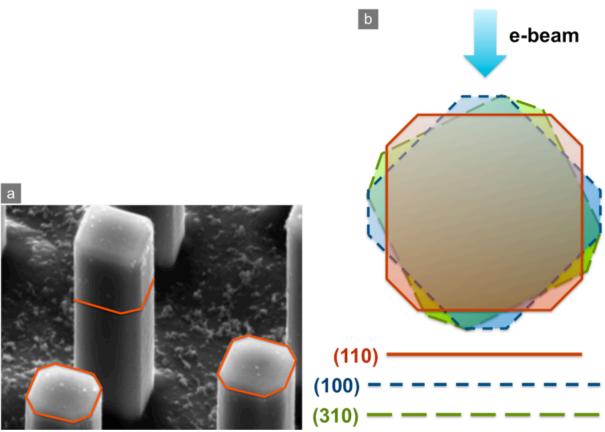
Figure 2.2.2: (a) SEM micrograph of Mo-alloy nano-fibers showing octagonal cross-section. Modified from [81]. (b) Schematic representation of rotational procedure in the TEM to determine CSA of the Mo-alloy nanofibers.

The raw force data is taken to be the force applied to the combination of the sample and the PTP device, and the raw displacement data is taken to be the motion of the flat-punch indenter. The spring constant of the empty PTP device used for these experiments was measured after sample fracture and found to be between 330 and 450 N/m, depending on the

device used. The force applied to the sample can be determined by subtracting the contribution of the PTP device from the raw force data. The engineering strain was calculated by dividing the raw displacement data by the initial gage length, measured in the SEM as the length between the two Pt grip pads. It must be noted that the calculated strain may be overestimated because the raw displacement is a homogenous representation of a heterogeneous sample strain. Additionally, the raw displacement may include not only the fiber displacement, but also any systemic compliance. The actual contribution of these errors is investigated and addressed in §2.4.

2.2.4 Calculating local true stress and strain

In-situ video was recorded with a 480x480 pixel resolution at 30 fps using a Gatan Orius 833 CCD camera. The true stress and strain at local areas of plasticity was directly calculated from the in-situ videos. Digital Image Correlation (DIC) was applied to the still frames extracted from the recorded videos to measure the local instantaneous projected width and the local elongation of the sample [82]. The cross-sectional area is assumed to reduce symmetrically, i.e. the <110> and <100> widths reduce by equal amounts, during plastic deformation. This symmetric reduction is indicated by SEM micrographs of deformed fibers after failure, such as seen in Figure 2.2.3, and used to calculate the local true stress. The local gage length was chosen individually for each fiber to be large enough to fully encompass the local area of interest. Surface features were typically used as markers for the DIC analysis to avoid any diffraction contrast effects as the fiber deformed. The location of the surface features also factored into the determination of the gage length used for each DIC analysis.
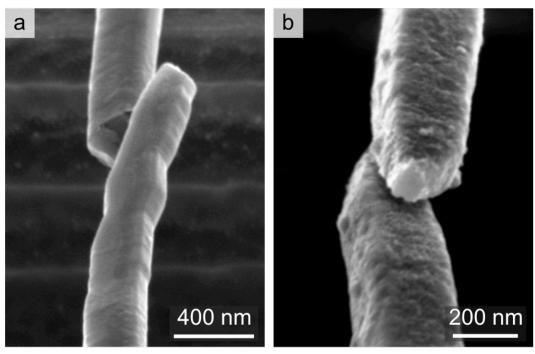
Figure 2.2.3: Post-mortem SEM micrographs of Mo-alloy fibers showing a symmetric cross section remains in a (a) 9% pre-strained fiber, and a (b) 15% pre-strained fiber.

2.3 Results and discussion of in-situ TEM mechanical tests

2.3.1 Source activation strength in Mo-alloy nano-fibers

At room temperature, the mobility of screw dislocations is much lower than edge or mixed dislocations and thus believed to control the overall rate of plastic deformation of bulk samples. Screw dislocation motion at room temperature is thought to be controlled by the nucleation and migration of kinks and kink-pairs[83], and cross-slip can easily occur, as any <111> oriented screw dislocation segment has three mutually intersecting (110) planes and three mutually intersecting (112) planes on which it can nucleate kink pairs and cross-slip[84]. Furthermore, Schmid's law, that slip will occur at a critical stress on the plane with the maximum resolved shear stress (MRSS), is known to break down in BCC materials; one consequence being a tension/compression flow stress asymmetry[85]. Thus, in-depth experimental analysis of dislocation behavior in BCC molybdenum is an inherently complicated 3-D problem. Accordingly, this section presents a focused investigation of source activation strength in Mo-alloy nanofibers.

The correlation of local true stress and the point of activation of a Frank-Read (FR) type source is compared to estimated stress using the dislocation radius of curvature, and a line-tension model of a large bow-out configuration. A 9% pre-strained FIB-free sample of a Mo-alloy nano-fiber was prepared as described in §2.1 and §2.2. All quoted experimental stress values are local true stress.

A two-node source was found in a fiber with measured projected <110> and <100> widths of 315 and 340 nm, respectively. The initial dislocation configuration before testing of the sample is one packet, as shown in Figure 2.3.1a. Upon uniaxial tensile loading, motion of the initial dislocations is first observed at 0.83 GPa. The dislocation source is observed to operate at least 2 times starting at 1.38 GPa, then again at 1.51 GPa, while initial and other generated mobile dislocations annihilate at the surface. However, the observation of slip traces generated after the first operation and at higher stresses, indicates some instances of initial pile up, likely caused by the 10 nm of surface contamination layer that is either an oxide residue from the etching process or Pt-C from diffusion of the grip-pad material. After the fiber is starved of large mobile dislocations, it suddenly fails at 2.29 GPa, without the sudden, large elongation seen in other fibers of similar initial dislocation densities.

Figure 2.3.2 shows the application of the fiber crystallographic geometry to propose the likely slip plane, slip direction, and source length. Slip traces were used to narrow the possibilities to either a (112) or (1-12) slip plane, and designate the position of the source within the fiber, assuming no cross-slip occurred. After-failure tilting was used to make a final determination between the two planes, and (112) was selected. However, this assumes the source is either responsible for the failure, or has the same slip system as the one that is. This is a reasonable assumption given recent TEM dislocation analysis of pre-strained Mo-alloy nanofibers that indicates lower dislocation dense fibers tend to have dislocations with the same slip system[69]. The source is mixed with b=a/2[-1-11](112), line direction 20° from the Burgers vector, and initial length of 177 nm. As seen in Figure 2.3.2, some outside force, such as image forces or anisotropy effects, or as a result of the mixed character of the dislocation, produce an asymmetrical dislocation shape. The left side of the dislocation has assumed a shape similar to Figure 1.2.2 b in §1.2.1 and the right has adopted a mostly edge character, aligning parallel to

the surface. Thus, the radius of curvature is taken from the leading edge of the bow-out near each node (Figure 2.3.2) and averaged between the two sides. By modifying equation 1.2.3, the radius of curvature can be used to measure the local applied uniaxial tensile stress

$$\sigma(R) = \frac{\mu b}{Rm} \tag{2.3.1}$$

where shear modulus $\mu = (c_{11}-c_{12})/2 = 129$ GPa (more details in §2.4), the magnitude of the burgers vector b = 0.2725 nm, R is the average radius of curvature of the dislocation, and m=.47 is the Schmid factor for the [-1-11](112) slip system. Table 2.3.1 shows there is good agreement, ~1% error, between the measured local true stress at points a-c (Figure 2.3.2), and estimation using the average radius of curvature. This is reasonably expected, as the dislocation shape necessarily includes the effects of self and outside forces.
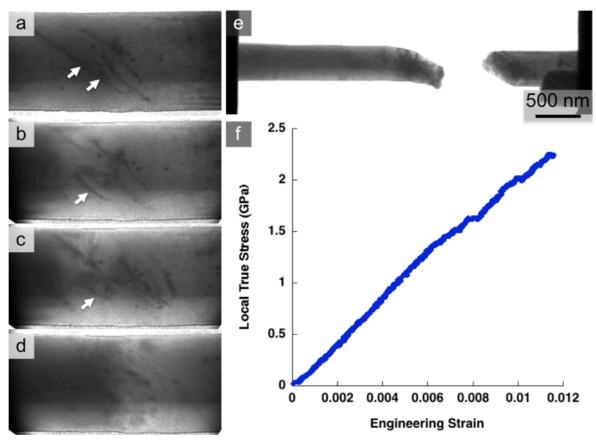
Figure 2.3.1: (a-d) Cropped stills from in-situ TEM video of 9% pre-strained Mo-alloy nanofiber. (a) At 0 GPa. White arrows indicate double node dislocation source. (b) At 1.19 GPa. White arrow indicates first visible dislocation bowing at a double-node source. (c) At 1.51 GPa. Arrow indicates second visible dislocation bowing at a double-node source. (d) At 2.00 GPa. Large mobile dislocations have been annihilated. Sessile loops and past slip traces can still be seen in the fiber. (e) TEM micrograph of failed fiber. 2.29 GPa. (f) Local true stress vs. engineering strain. True stress was calculated using DIC, however DIC was not successful in tracking strain.
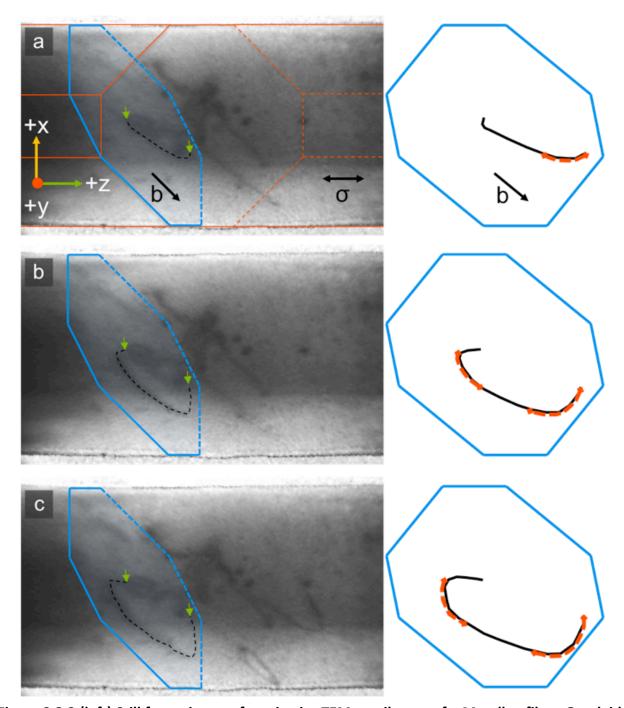
Figure 2.3.2 (left) Still frame images from in-situ TEM tensile test of a Mo-alloy fiber. Overlaid in red are the fiber edges and CSA shape. Shown in blue is the (112) plane. (right) Corresponding view of (112) and dislocation as seen if parallel to the page. Red dashed lines indicate where radius of curvature was measured. (a) σ=1.13 GPa. A mixed dislocation, b=½[-111](112), is pinned between two points (green arrows). (b) σ=1.19 GPa. As the stress increases, the dislocation bows out. (c) σ=1.38 GPa. Final frame before the dislocation source activates, leaving another dislocation between the two nodes, and operating at least once more.

Table 2.3.1: Local stress calculations at points corresponding to Figure 2.3.2, using the radius of curvature method and indenter measurements of local true stress. Right and left refer to the node the dislocation section is closest to.

Image	σ (GPa) (radius of curvature method)			σ (GPa) (measured)
	Right	Left	Average	
a	1.15	N/A	1.15	1.13
b	1.32	1.09	1.21	1.19
c	1.39	1.39	1.39	1.38

Though the source starts as a double-pinned dislocation, Figure 2.3.2 indicates the area may be too limited for the bowed dislocation to spiral around both pinning points and generate a loop, as in the F-R source. If this is the case, the dislocation intersects the fiber surface and becomes two spiral sources, operating at a lower stress. However, if the 10 nm surface contamination material were a strong enough slip barrier, the mechanism could continue as a F-R source. Accordingly, both options will be considered.

The expression for the local applied uniaxial tensile stress required to activate a F-R-type source, or to bow a dislocation to a critical size, as a function of source length, L, can be found by modifying equation 1.2.6 with the Schmid factor, m, of the slip system to

$$\sigma(L) = \frac{1}{m}\left[\frac{\alpha\mu b}{L} + \tau_{ex} + \tau_{O}\right].$$

(2.3.2)

The sum of the external, τ_{ex}, and friction stresses, τ_o, can be estimated by noting the onset of dislocation motion in the experiment, which was 0.827 GPa for this fiber. Here, the source strength coefficient of a F-R source, α, using a line tension consideration of a large bow-out configuration has been calculated as[12]

$$\alpha = \frac{1}{2\pi(1-\nu)}\left\{\left[1 - \frac{\nu}{2}\left(3 - 4\cos^2\beta\right)\right]\ln\frac{L}{\rho} - 1 + \frac{\nu}{2}\right\}$$

(2.3.3)

where ν=0.28 is the Poisson's ratio, β=20° is the angle between the Burgers vector and the dislocation line, and ρ is a cutoff parameter set equal to the Burgers vector.

It has been shown that the source strength coefficient of a spiral, or single-node, source is about 0.5x that of a F-R, or two-node, source, and screw sources are ~1.5x stronger than edge sources[12,86]. Source strength coefficients and activation stresses for different dislocation configurations were calculated using eqns. 2.3.2 and 2.3.3, and are presented in Table 2.3.2. If the point of source activation were taken to be the point right before the bowed half-loop becomes unstable, as in Figure 2.3.2c, and does operate as a mixed F-R source, then the error of the predicted activation stress with respect to the measured local true stress is 1.2% and 0.4% difference using the stress measured by the radius of curvature.

Table 2.3.2: Calculated source strength coefficients, α, and source activation stresses, σ, for Frank-Read and single-node sources of length L=177nm, using eqns 2.3.2 and 2.3.3.

	Frank-Read			Single-Node $\alpha_{SN}=\frac{1}{2}\alpha_{FR}$		
	Screw	Edge	Mixed β=20°	Screw	Edge	Mixed β=20°
α	1.447	0.638	1.352	0.724	0.319	0.676
σ (GPa)	1.438	1.096	1.398	1.132	0.962	1.112

It is highly promising that the predicted and radius-of-curvature calculated stresses are so close to the measured local true stress. First, this implies there is no intrinsic size effect at this size scale and can be directly related to bulk properties, and two, to use local true stress measurements, rather than radius of curvature, one does not have to rely on knowing the true shape of the dislocation, or needing a dislocation at all, for stress analysis. This also allows for direct comparison of experimental values to models. The applications for such a sensitive quantitative measurement of stress and strain are numerous, allowing experimental study of such things as surface effects, source truncation hardening, and defect interactions. Unfortunately, the speeds at which deformation mechanisms operate are often beyond the ability of present recording technology to capture. Improvements in camera technology, an example of which is used in §2.3.2, are a necessary step in probing fundamental mechanical behavior of materials.

2.3.2 High temporal resolution in-situ TEM tensile experiment

The origin of size-dependent yield stresses in small-scale samples, whether the increased strength is due to the stochastic nature of defects or new failure mechanisms, is still debated. Simulations easily access the nano size scale and can control individual phenomena, such as image stress and dislocation core structure, but without physical evidence, conclusions remain theoretical. One notable computational investigation of deformation of small-scale samples, by Weinberger and Cai, predicts a new size-dependent deformation mechanism in BCC materials: surface-controlled dislocation self-multiplication[87]. Combining discrete dislocation dynamics (DD) and molecular dynamics (MD) simulations, it was found that by accounting for surface effects on the strain field and dislocation mobility, a single dislocation nucleation event can quickly populate a pillar, under uniaxial compression, with dislocations. Experimental evidence of this phenomenon is thin, however dislocation free Mo pillars[37] and as-grown Mo-alloy nano-fibers[81] have been seen to suddenly catastrophically deform under compression at high stresses. Experimentally, uniaxial compression is very hard to achieve, as the taper of FIB-machined samples leads to stress concentrations near the tip. This introduces uncertainties in measured activation stress needed for comparison to the model. Here the experiment has been replicated for uniaxial tension using a 30 fps and 400 fps camera with the hope of capturing some evidence of the sudden failure mechanism.

The first Mo-alloy nano-fiber, Figures 2.3.3 and 2.3.4, was prepared as discussed in §2.1 and §2.2, and mechanically tested in-situ in a JEOL 3010 TEM at 300 keV. The test was recorded with a Gatan Orius 833 CCD camera at 30 fps, and more details of the results can be found elsewhere[49]. The fiber has a measured projected <110> width of 336 nm, and a calculated <100> width of 327 nm. DIC was successful for this test, however in order for comparison to the

second fiber to be made, where DIC was not successful, the engineering stress-strain curve is presented in Figure 2.3.3b. During deformation, the four initial mobile dislocations (Figure 2.3.4a) start to move at a stress of 387 MPa, and annihilate one by one. Later, slip traces can be seen on (112) and (-112) planes, disappearing after interacting with the surface layer and leaving visible steps, or 5-10 dislocations (Figure 2.3.4b,c). One (-112) slip trace appears to have a dislocation source (Figure 2.3.4c), however this plane is nearly parallel to the electron beam and cannot be analyzed. The dislocation-exhausted fiber suddenly elongates at an engineering stress of 2.98 GPa, or calculated local true stress of 3.00 GPa, on the (-112) plane. Figure 2.3.3a shows 4 successive frames of the failure event, or lack thereof. Despite slip traces on more than one slip plane, post-mortem SEM investigations indicate one primary slip system responsible for the failure, [1-11](-112), as the portion of the fiber between the two diagonals retains the original thickness of the fiber, and accounts for nearly all the induced strain. The sudden strain event produced a final 1.2% strain along the <001> loading direction, or 725 dislocations, in less than 1/30th of a second. For a single node source, this is a dislocation production rate of at least 2×10^4 s^{-1}, which corresponds to an average velocity of a spiral source tip of 2 cm/s, which is reasonable[83,88,89]. Post-mortem tilting shows few dislocations in the thinner portion between the two slip surfaces of the fiber, and few dislocations extending past the failure planes. This implies little pileup or dislocation interaction, for a fast-operating source.

The opportunity to observe deformation mechanisms at 400 fps was made with the development of the Gatan K2-IS direct electron detector camera. A second Mo-alloy fiber, shown in Figure 2.3.5, with no observable initial defects, was prepared in the same way and mechanically tested in-situ in an FEI TitanX using a Hysitron PI-95 indenter for FEI microscopes. The fiber has a measured projected <110> width of 293 nm, and a calculated <100> width of 293 nm. This fiber fails at 2.40 GPa engineering stress after minimal plasticity that was only seen by the stress-strain curve. DIC was not attempted for this experiment, as there are few surface features to use in tracking. However, the local true stress and strain are assumed to be very similar to the engineering stress and strain as there was little observable plastic deformation. The local true failure stress was found using the frame before failure and calculated to be 2.43 GPa, and the slip system responsible for failure appears to be [111](-1-12). The K2 camera allows observation of the fiber before the indenter feedback loop returns the sample to the pre-strain burst position, which compresses the two ends. In contrast to the first fiber, which appears to remain intact with one source responsible for continuously displacing material, the second fiber fully fails and appears to have two discrete slip locations. Two separate primary slip locations, with the same slip system, are proposed as a consequence of three observations: one, that two necking points are present and unrelated to later buckling, two, the material between them is free of dislocations, and three, the length between them is greater than the total strain. The total strain produced is 1.0% along the <001> loading direction, or 375 dislocations, in less than 1/400th s. For two sources, this is a dislocation production rate of at least 8×10^4 s^{-1} per source, which corresponds to an average velocity of a spiral source tip of 8 cm/s, which is reasonable. Unfortunately, the deformation mechanisms involved in this failure were still not observed, despite the increase of frame rate from 30 to 400 fps, and possible deformation mechanisms of the two fibers are explored below.

The surface-controlled self-multiplication model requires the applied stress to surpass the back-stress of the dislocation curvature to keep the surface nodes moving so that a cusp, created by the motion of surface-nucleated kinks of a single dislocation, can develop into a loop, thereby creating two new dislocations, and at higher applied stresses can each in turn create their own loop, and so on. In their paper[87], Weinberger and Cai fit the molecular dynamics (MD) and discrete dislocation dynamics (DD) simulation data of the critical stress required for this mechanism as a function of sample size for compression tests of molybdenum pillars as

$$\sigma(D) = \frac{A}{D}\ln\left(\frac{D}{B}\right),$$

(2.3.4)

(henceforth referred to as the W-C model) where D is the diameter of the cylindrical sample, A= 57.5 GPa, and B= 0.835 nm. If the diameter of the experimental Mo-alloy nano-fibers is taken to be the average of the <100> and <110> projected widths, the critical stress for loop formation for the first fiber is 1.04 GPa and 1.15 GPa for the second, which are below the experimentally measured local true stress values of 3.0 and 2.44 GPa, respectively. The discrepancy could be due to other unapparent hardening mechanisms in the Mo-alloy tensile experiment, such as the alloying elements or the 10 nm surface contamination layer. Thus, the calculated critical stress should be thought of as a lower bound, and the larger the discrepancy, the larger the likelihood of a dislocation avalanche, where the dislocations created by the cusp-to-loop formation create their own loops, quickly populating the sample with dislocations. Additionally, though the W-C model is isotropic, similar shear modulus and Poisson's ratio, 123 GPa and .305, are used. One problem in comparing this model to the present experimental observations is the model is in compression, and these tests are tension. This is particularly important for {112} slip systems, due to the flow stress asymmetry that may be present[90]. And finally, though the shape of the Mo-alloy nanofibers is a hexagonal prism, a good approximation of a cylinder, the image forces and surface effects are likely more complex. Analysis of the lower fracture surface of the first fiber (Figure 2.3.3a for frame of reference) shows there are three parallel (-112) slip planes (white dashed lines in Figure 2.3.4 separated by (011) cross-slip planes (black dashed lines), with dislocation loops present on both of the mutually intersecting (121) and (-2-11) planes (Figure 2.3.4d). Further along the slip direction, seen as the thinner portion in Figures 2.3.3a and 2.3.4d, the slip evens out, with the appearance of single slip on the (-112) plane, and few dislocations. Above a critical temperature of 60K, the slip steps of screw dislocations are expected to be equally frequent on mutually intersecting {112} planes, which may appear as having an effective {110} plane[91]. As such, the (011) cross-slip along the fracture surface is likely to be equal cross-slip on the mutually intersecting (121) and (-2-11) planes, similar to the W-C model, which fixes the surface nodes on two different mutually intersecting {112} planes. This is then possible experimental evidence for the W-C model, as the fracture surface can be explain thusly: a single dislocation is nucleated with surface nodes on the (1-21) and (-211) planes; next, because the applied stress is 3x the W-C critical stress, the initial debris loop created results in a strain avalanche; then, some of these multiplied dislocations interact, forming nodes for a source, such as a Frank-Read source, which carries the rest of the strain more evenly on the (-112) plane, resulting in the thin section between slip surfaces with few residual dislocations. Unfortunately, the slip of the second fiber, recorded at 400 fps, occurred

with a projected slip plane nearly orthogonal to the viewing direction, making analysis of the fresh fracture surface before it is compressed by the other sample half, impossible.

Another collective dislocation motion mechanism, that could explain the sudden strain softening and the presence of two necking points, is the Portevin-Le Chatelier (PLC) effect[92]. The PLC effect primarily presents as serrated stress-strain curves, or load drops, of materials, usually alloys. In this instance the mechanism as it presents as plasticity band propagation is considered. For the present experiments, the mechanism requires the presence of dislocations. Thus, in the first phase of the mechanism, Mo-alloy nano-fibers must first nucleate dislocations; in the second phase, the dislocations are unpinned from the solute clouds, aluminum and nickel in the case of the Mo-alloy nano-fibers; in the third phase there is rapid dislocations glide towards the middle of the sample in the form of a band[93], at propagation velocities on the order of 100 μm/s[94]; in the fourth phase the dislocations are recaptured and pinned at some forest obstacles, this location would be on the top (Figure 2.3.3) of the much thinner section of the first fiber and the second necking point to the left in the second fiber (Figure 2.3.5). In each fiber the distance between the initial and final band locations is ~500 nm, for a band propagation velocity ≥15 and ≥200 μm/s for the first and second fiber, respectively, which are reasonable[94]. Additionally, non-dislocation, structural mechanisms could be responsible for the sudden strain events such as twinning[83], reversible twinning[95], or a reversible high-stress BCC to FCC phase transition[96]. Though these will not be explored here as the focus is on dislocation mechanisms.

Despite major advances in in-situ imaging technology, the deformation mechanisms at play in nano-scaled BCC materials happen at incredibly fast speeds and could not be directly observed and confirmed, even at a sampling rate of 400 frames per second. This leaves much room for data interpretation, and if these surface or high-stress driven mechanisms are energetically favorable or more likely at the nano-size and the much higher stresses of nano-scale experiments, it could pose a problem in extrapolating to bulk-scale mechanical behavior. Thus, high temporal resolution TEM experiments, perhaps achieved with Dynamic TEM (DTEM)[97], may be needed for further investigation.
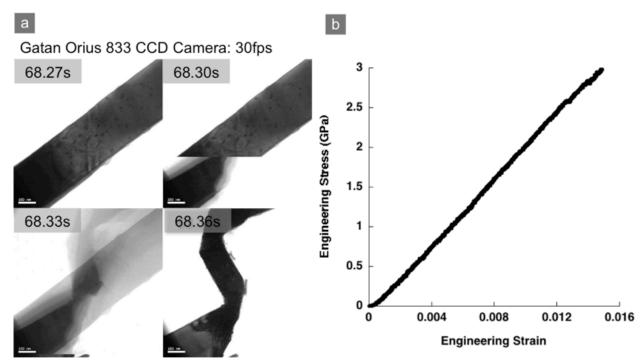
Figure 2.3.3: (a) Successive still frames from Gatan Orius CCD camera in-situ TEM video of a Mo-alloy fiber recorded at 30 fps. (b) Engineering stress strain curve. DIC was successful for this fiber, however to compare to the fiber in Figure 2.3.4, engineering values are used. Image modified from [49].
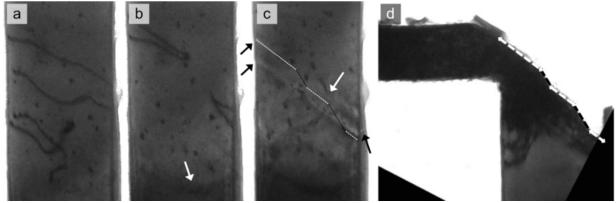
Figure 2.3.4: Rotated and cropped still frame images of in-situ TEM tensile test recorded at 30 fps. (a) The dislocation structure a frame before the first dislocation moves at σ_{eng}= 387 MPa. (b) After the two lower dislocations have annihilated the two left are briefly pinned by sessile loops. The white arrow indicates a (112) slip trace. (c) Frame before failure, σ_{eng}= 2.98 GPa. The left black arrows indicate slip steps, resulting from 5-10 dislocations on the primary slip system, [1-11](-112). The black arrow on the right indicates where the dislocations have interacted with the surface contamination layer to clear the slip trace. A dislocation source can be seen in the (-112) plane, which is nearly parallel to the electron beam (white arrow). The resulting failure surface position is overlaid using dashed lines. The primary slip plane, (-112), is shown in white and the (011) cross-slip plane in black. (d) After fracture, the surface planes (dashed lines) are correlated to the previous image. Some images modified from [49].

25
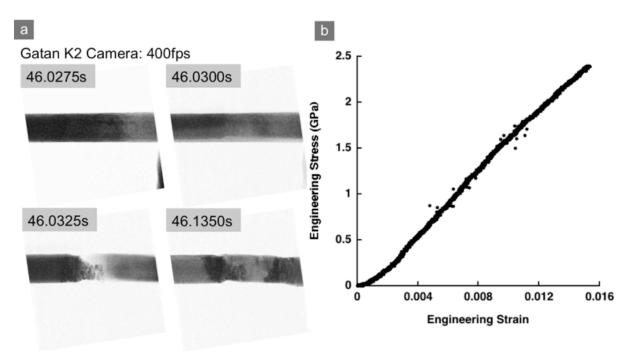
Figure 2.3.5: (a) Still frames from Gatan K2 camera in-situ video. Three consecutive frames show no observable dislocation activity at the time of failure, however two individual necking points are observed. (b) Engineering stress strain curve. DIC was not attempted for this experiment

2.3.3 In-situ TEM tensile tests of unirradiated and irradiated Mo-alloy

The development of advanced computational methods that can be used for predicting performance lifetimes of materials exposed to harsh radiation environments are highly dependent on our fundamental understanding of solid-radiation interactions that occur within metal components. As these computational methods expand their time and size frames, the focus becomes defect interactions, and how they drive the mechanical response of materials under extreme environments. To study isolated single irradiation defect interactions, the microstructural evolution must be highly controlled or characterizable. For decades, in-situ TEM irradiation has allowed for the direct correlation of defect evolution as a function of irradiation[15], and affords more control over the resulting microstructure than ex-situ irradiation, with room for improvement. As a result, the experimental comparison of unirradiated and irradiated mechanical deformation mechanisms presented here is a study of collective, rather than isolated, defect behavior. The hope is future advances in technology, for example He-ion FIBs, allow for more highly focused microstructural control.

To provide a frame of reference for the typical collective defect response of unirradiated Mo-alloy nanofibers, a brief overview of the mechanical behavior when varying size and initial dislocation density is presented, followed by the comparison of the mechanical response of irradiated to unirradiated Mo-alloy fibers. Mo-alloy nano-fibers of varying dislocation densities and sizes have been mechanically tested by ex-situ nano-indentation[31,65,98] and compression[54,81], in-situ SEM tension[28,99], and in-situ TEM tension[49]. A fiber with no initial dislocations, as in Figures 2.3.6a and 2.1.2.a, will fail under tension by sudden elongation. The

26

smaller as-grown fibers tend to fail at higher stresses, however, no systematic study of size dependence in tension has been done, and compression experiments show no strength size dependence for as-grown fibers[54]. This discrepancy may be due to the larger surface sampling in tension. In-situ SEM tensile tests show large scatter, 1-10 GPa, in yield strength for gage lengths around 10 μm for as-grown fibers, and deterministic behavior at very small and very large gage lengths[28]. At intermediate dislocation densities, 4-9% pre-strain (Figure 2.3.6b), the fibers generally have only a few longer dislocations and dislocation debris loops. As seen in §2.3.2 (Figure 2.3.3), the onset of plastic behavior begins around 1.4 GPa, which compares well to the results for compression of 8% pre-strained fibers reported elsewhere[54]. Intermediately pre-strained fibers generally fail by sudden elongation on {112} plane with some evidence of (110) cross-slip, which may actually be the effective plane of two equally active mutually intersecting {112} planes. Intermediately pre-strained fibers with initial dislocation sources that activate at lower stresses also fail suddenly, but with a much more moderate strain burst (Figure 2.3.1 §2.3.1). In comparison to compression studies, which show a wide range of failure stresses for intermediately pre-strained nano-fibers of a given size, these in-situ TEM tensile studies have little spread in yield strength, ~1.4 GPa, and ultimate strength, ~2.5 GPa, for fibers ~300 nm wide. This may be a consequence of the ability of the TEM to identify whether or not there are initial dislocations. As discussed elsewhere[49], the tensile response of fibers with high initial dislocation densities (Figure 2.3.6c), is similar to less pre-strained fibers only in that plastic behavior begins around 1.4 GPa, and ultimate strengths are near 2.5 GPa. In contrast, tensile straining of heavily dislocated fibers results in single necking, or plastic instability, points with very large resulting reductions in area, stress-strain curves that show several large load drops, and slip systems that appear to be <111>{110}. Highly pre-strained fibers also show that, though the failure strains are certainly below typical total elongation values of ~20%[100], the heavily dislocated fibers are more ductile than their less dislocated counterparts. The traditional view of work hardening is that it is achieved by increasing the number of dislocations; this increases the density of forest dislocations, which require greater stresses to overcome. This seems to be the opposite in samples of this size regime, where dislocations can more easily escape to the surface and hardening is instead due to mechanical annealing, an observation made in these tensile experiments as well as in-situ TEM compression[101]. However, the result is the same: there are fewer mobile dislocations.

Clearly, defect density, and likely sample size, affects the mechanical behavior at these size scales. Thus, a direct comparison of the mechanical behavior of an irradiated Mo-alloy nanofiber to the behavior of unirradiated material necessitates a comparison to the mechanical response of a fiber with similar size, shape, and initial defect density. It is then possible to explore any change in mechanical behavior exclusively as a function of defect origin.
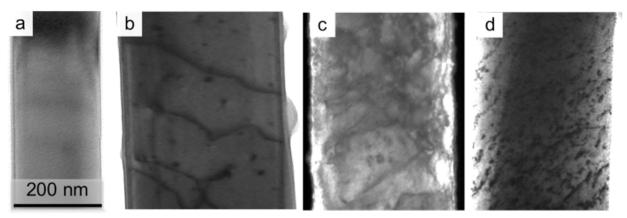
Figure 2.3.6: TEM micrographs of Mo-alloy nanofibers. (a) 0% pre-strained, no dislocations or observable defects. (b) 9% pre-strained with mobile dislocations and sessile loops. (c) Dark-field micrograph of 15% pre-strained fiber. (d) He[1+] and Ni^{2+} irradiated, 9% pre-strained fiber.

A 15% pre-strained nanofiber, shown in Figure 2.3.7, with initial dislocation density of 1.6×10^{14} m^{-2}, <110> and <100> edge widths of 244 and 290 nm, respectively, was prepared according to the procedures outlined in §2.1 and §2.2. The dislocation density was calculated according to Ham's method[68], as discussed in §2.1.3, and more details regarding this nano-fiber can be found elsewhere[49]. Figure 2.3.7f shows the successive loading and unloading of the fiber done four times. Such a cyclic test was not the initial intention, but was necessary after taking a conservative approach to testing, and the fiber surpassing elongation expectations. The curves are arranged such that the elastic loading of the next test corresponds to the elastic unloading of the previous in order to simulate the behavior of a single tensile test. The data follows typical work hardening behavior, where the yield point of the next test is near the highest stress reached previously. Test 3, shown in yellow in Figure 2.3.7f, begins plastic behavior at a higher stress than expected, which is likely due to the onset of necking. Unloading after the sample has begun to neck acts to compress the sample, further clearing dislocations. This is in contrast to the typical work hardening mechanism in that the hardening is due to a decrease, rather than an increase, in dislocation density. The load-displacement data between successive tests was found to correspond more closely than the engineering stress-strain data, appearing as a single test (Figure 2.3.10a). Dislocation motion is first observed at 0.73 GPa, before the onset of plastic behavior at 1.38 GPa (Figure 2.3.7b). The sample begins to neck at 2.08 GPa (Figure 2.3.7c), after which there is sustained plastic deformation accompanied by hardening, and later, simultaneous slip events leading to load drops, as seen in Figure 2.3.7d. Yield followed by sustained plasticity corresponds well with what has been observed previously in compression tests of highly pre-strained Mo-alloy pillars[54].

A 9% pre-strained nanofiber, shown in Figure 2.3.8 was concurrently implanted with 10 kev He[1+] and irradiated with 2.8 MeV Ni^{2+} in-situ in the I[3]TEM at Sandia National Laboratory, as outlined in §2.1.4. Preparation of a tensile sample with primary irradiation defects of b=a/2<111>{110} type interstitial and vacancy loops (see §2.1.4), was done according to the procedure in §2.2. The sample dimensions are 242 and 281 nm for <110> and <100> edge widths, respectively. This is only a 3% difference in CSA between the unirradiated and irradiated fibers presented here. Defect cluster density was calculated to be 2.7×10^{22} m^{-3} according to the

method outlined in §2.1.4, and a correlating dislocation density of 4.5×10^{14} m^{-2} calculated according to Ham's method (§2.1.3). The tensile testing of this fiber was performed using the Hysitron PI-95 ECR holder, and the noise in the data is believed to be electrical in nature, rather than mechanical vibration. Unfortunately, this results in the obfuscation of any small changes in data. It is worth noting the data of the unirradiated fiber becomes as noisy in Test 4; however this is vibrational, the source of which is unclear. The frame rate of the video recording was reduced to 15 fps to increase contrast that was reduced by the many irradiation defects. Unfortunately, the decreased frame rate makes it less clear when dislocations first move, though it appears to be between 0.73 and 0.92 GPa, again before the onset of plastic behavior at 1.52 GPa. Necking begins at 2.41 GPa, after which there is sustained plastic deformation accompanied by hardening and slip events leading to load drops, similar to the unirradiated fiber. It is interesting the mechanical behavior, regardless of defect origin, so closely matches.

Comparisons of the load-displacement and engineering stress-strain curves of the two fibers, Figure 2.3.10, show remarkably similar behavior. They each have similar yield points, maximum engineering stress reached, number and size of load drops, and onset of necking strains. Each exhibits continuous plasticity until ~5% strain, whereupon intermittent strain bursts in the form of load drops begins. Though the irradiated fiber is expected to have more point defects and defect clusters below the resolution limit of the microscope, the only indication of their presence is in the increase in initial stress to move a dislocation, however the reduced frame rate and noisy data makes the exact difference difficult to quantify. It can also be said that the strain was more localized in the unirradiated fiber, as it achieved a larger reduction in area per strain, however this may be an effect of having a longer gage length (8.2 vs. 5.6 µm).

One downside to displacement controlled testing is highlighted by both these samples in Figure 2.3.9. The tensile tests runs according to a pre-set loading/unloading profile that cannot be altered during testing, which can lead to the frustrating result of not quite reaching the point of failure. For both these samples this resulted in failure during unloading, as the sample buckles at the necking point. The local true stress was not calculated for either sample due to load drops and/or sample vibration, which resulted in many blurred single frames, making DIC intractable. Fortunately, it is unnecessary for the present study of collective defect behavior to have local stress measurements. Though, the true stress reached at the necking point before unloading for the fibers can be calculated from still frame images of the video recording. The unirradiated fiber achieved a 74% reduction in area for a true local stress at the necking point of 5.1 GPa, and the irradiated fiber achieved a 64% reduction in area and local true stress of 3.8 GPa. As neither test was taken to failure during tensile strain, it is unknown to what extent the reduction in area and total elongation may have been.

The primary slip system, though many are active as evidenced by the nominal preservation of the original cross-sectional shape (Figure 2.2.3b §2.2)), for both fibers is <111>(10-1). This is in contrast to the lower dislocation density fibers presented previously, which have <111>{112} slip systems. This difference can have one or both of two origins; the first implies an inherent difference in behavior of the irradiated fibers, and the other implies no difference. TEM analysis and tomography[69] show the dislocation structure of pre-strained fibers is primarily b=a/2<111>{112} dislocations with varying degrees of cross-slip, and small loops that are primarily prismatic debris loops, a feature also confirmed via simulations[83,89]. To

overcome the increase in defect barriers, the dislocations of the heavily dislocated fibers increase the amount of dislocation cross-slip along mutually intersecting {112} planes, which can appear as a single {110} plane, depending on the step size. In contrast, the defects of the irradiated fiber are primarily b=a/2<111>{110} interstitial or vacancy loops (see §2.1.4 for more details). These loops may either slip accordingly, or like the unirradiated fibers, cross-slip on mutually intersecting {112} planes in elementary slip steps that result in the appearance of a {110} primary slip plane.

A low temperature neutron irradiation study of bulk polycrystalline Mo, by M. Li and coauthors[102], shows a complicated interplay between sample temperature, strain rate, and irradiation dose. The mechanical behavior is non-linear, with strength and ductility initially softening then hardening with increasing dose, similar to the Taylor hardening model where the yield strength follows a $\sigma=\rho^{-1/2}$ dependence to dislocation density. By correlating the size and number of visible defects created by ion irradiation, implantation, and room temperature anneal in the irradiated fiber to the size and number created by neutron irradiation, the mechanical behavior can then be correlated to the results of low-temperature neutron irradiation by Li, et. al. Defect cluster density is estimated to be 2.7×10^{22} m^{-3} which correlates to a neutron dose in the Li, et. al. study of 3×10^{-3} dpa, when considering the minimum resolved cluster size to be ~10 vacancies. The neutron irradiation experiment shows that at room temperature and a neutron dose of 3×10^{-3} dpa, the mechanical behavior of irradiated bulk polycrystalline Mo is very similar to its unirradiated counterpart. From their data the yield strength, total elongation, plastic instability stress (the true stress at the ultimate tensile stress point), are expected to be the same for a given temperature and strain rate. The unirradiated %RA is expected to be slightly higher than the irradiated, as was seen here, and surprisingly their 3×10^{-3} dpa data is noisier as well, though the authors do not give an explanation as to why. Their data also gives an explanation for the slightly higher strength of the irradiated fiber seen here: though both fibers were deformed at the same displacement rate, 2 nm/s, the irradiated fiber was strained at a slightly higher strain rate, 3.6×10^{-3} vs 2.5×10^{-3} s^{-1}. This all implies that the irradiation-induced defects in this Mo-alloy nanofiber are at the cusp of being thermal or athermal dislocation motion barriers. Though, because the fiber started with a, presumably, lower dislocation density, it is likely to have formed as many athermal barriers as the 15% pre-strained fiber has.

This set of in-situ TEM tensile experiments show that collective defect behavior, regardless of defect type, can lead to similar mechanical properties; and neutron irradiation experiments have shown mechanical behavior is dependent on several factors and follows a Taylor-hardening-like model, thus a range of temperatures, strain rates, doses, etc. must be done to obtain the overall behavior of irradiated Mo-alloy nanofibers. These complications can be avoided and fundamental behavior can be explored with a detailed analysis of the initial, transitional, and final dislocation structures of irradiated Mo-alloy tensile specimens, perhaps using 4-D electron tomography, provided the initial defect structure can be more finely controlled.
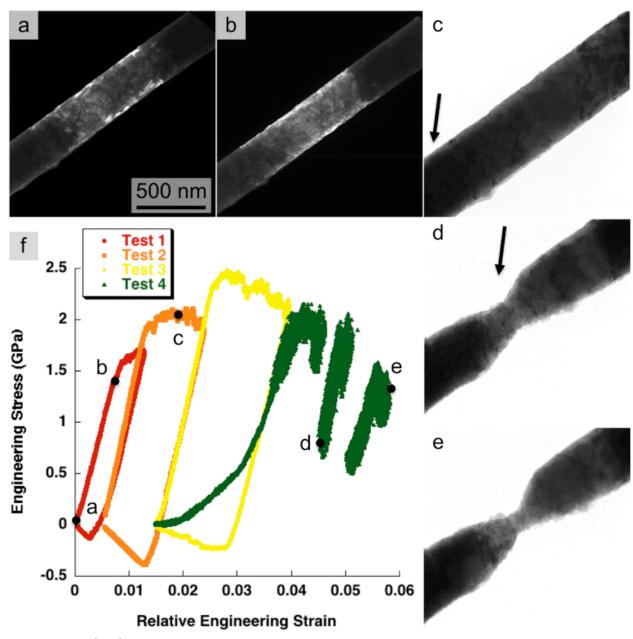
Figure 2.3.7: (a-b) Still frame images from in-situ TEM tensile tests of 15% pre-strained fiber in dark-field and **(c-e)** bright-field. **(a)** 0 GPa Initial dislocation structure. **(b)** 1.38 GPa Onset of plastic behavior. **(c)** 2.08 GPa Onset of necking, indicated by black arrow. **(d)** Resulting microstructure after a load drop from 2.00 to 0.82 GPa. The sample has been repositioned, such that the black arrow corresponds to the black arrow in (c). **(e)** 1.33 GPa Final microstructure before unloading.
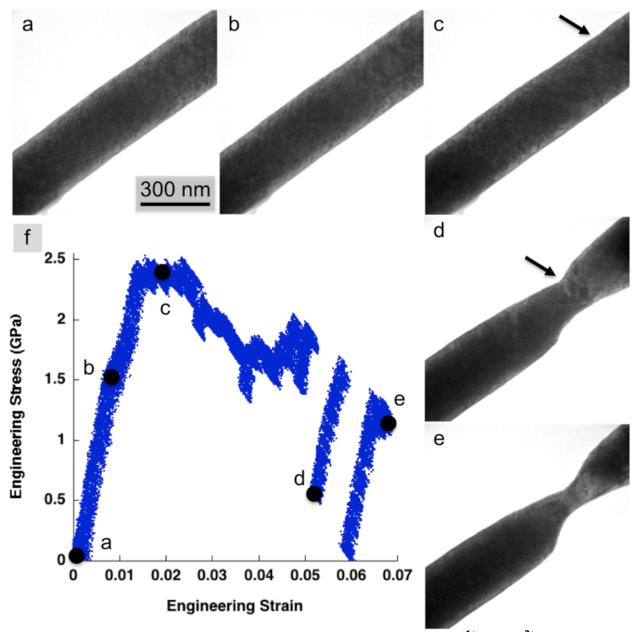
Figure 2.3.8: (a-e) Still frame images of in-situ TEM tensile test of He^{1+} and Ni^{2+} irradiated 9% pre-strained Mo-alloy nanofiber. (a) 0 GPa Initial microstructure. (b) 1.52 GPa Onset of plastic behavior (c) 2.41 GPa Onset of necking, with the black arrow indicating the necking point. (d) Resulting microstructure after a load drop from 1.85 to 0.52 GPa. The electron beam has been shifted rather than the sample, such that the black arrow corresponds to the black arrow in (c). (e) 1.34 GPa Final microstructure before unloading.
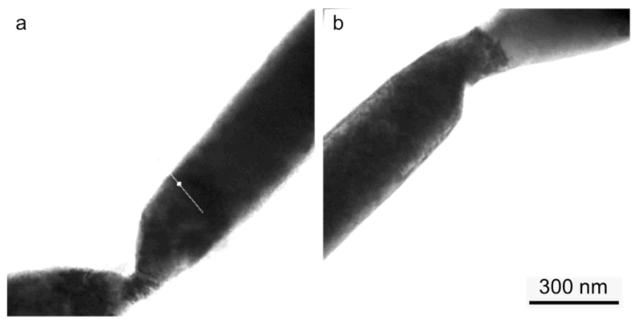
Figure 2.3.9: Bright-field TEM micrographs of (a) unirradiated 15% pre-strained and (b) irradiated 9% pre-strained fibers, after their respective tests failed to take them to tensile failure, causing buckling at the necking point. The white line in (a) is from a real-time measurement of the necked region and does not indicate anything here.
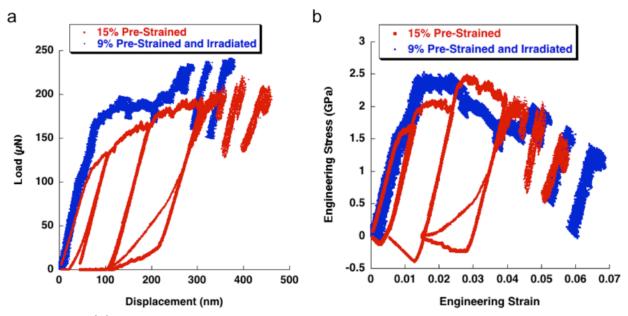
Figure 2.3.10 (a) Load vs displacement for the 5 successive tensile tests of the unirradiated and irradiated Mo-alloy nano-fibers. (b) Engineering stress vs engineering strain for the two fibers. Note the similar yield points, maximum engineering stress, number and size of load drops, and plastic instability strain.

2.4 Experimental error

Collected properties of the Mo-alloy nano-fibers presented in this chapter, and two presented elsewhere[49] are presented in Table 2.4.1. The Young's modulus of these fibers is 226±17 GPa, averaged over all initial and subsequent tensile tests (Figure 2.4.1). If only the initial tests are considered, the average Young's modulus is 217±3GPa. The calculated anisotropic elastic modulus of the Mo-alloy nano-fibers along the <001> direction is 328±15 GPa, using the rule of mixtures to include effects of the alloying elements Al and Ni[12,98,103–113]. Lower-than-bulk measured moduli are not uncommon in small-scale samples. Kiener and Minor remark specifically on this observation of their nano-tensile test of copper, which only measures 52% of the calculated modulus[114]. They cite dislocation motion outside the gage section, compliance of the load frame, easily mechanically annealed surface defects, and misalignment of the sample as possible sources of error. These Cu samples were FIB-shaped dog-bones and pulled directly with the PI-95, eliminating the need for Pt grips. Murphy, et. al. explore the compliance of EBID-Pt grips used in in-situ SEM nano-tensile tests of several single crystalline materials[115]. Using DIC, the actual strain of the samples was measured and used to calculate the compliance of the Pt grips. They found using DIC-measured strain corrected for the average modulus error of 19%. A similar observation was made when tensile testing as-grown Mo-alloy nano-fibers in the SEM. Johanns, et. al. found Young's modulus increased from 215 to 295 GPa when using DIC measured strain of tracked Pt pads, excluding machine compliance, to 320 GPa when using DIC to track points on the fiber, presumably excluding both machine and Pt grip pad compliance[28]. They further cite possible errors in CSA measurement due to contamination layer buildup. This section will address these possible sources of modulus error and additional ones unique to the setup used. A 9% pre-strained Mo-alloy nano-fiber with added engineered markers, 15 nm diameter Au nano-particles, was chosen to investigate and address these sources of error (Figure 2.4.2). The <110> and <100> projected widths were measured to be 296 and 298 nm, respectively, and symmetry of the fiber was confirmed over a full 60° of sample tilt. In order to provide a reference for presentation of results, this and previously presented fibers are henceforth referred to as numbered from F1-F8, as shown in Table 2.4.1.
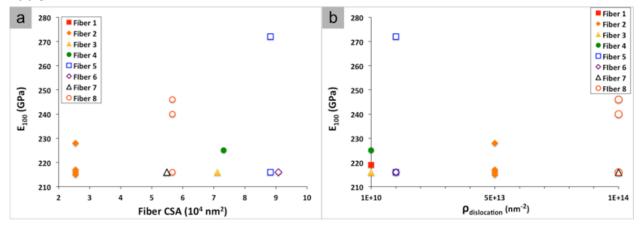
Figure 2.4.1: Measured Young's modulus of Mo-alloy nanofibers along the <001> growth axis of the fibers versus (a) cross sectional area and (b) dislocation density. Initial tensile tests

measure an average modulus of 217±3 GPa. Subsequent testing increases the measured modulus. Fiber numbers referenced as shown in Table 2.4.1.

Table 2.4.1: Consolidated Mo-alloy nano-fibers with associated properties, presented in Ch. 2.

Fiber	Images	% Pre-Strain	$\rho_{dislocation}$	CSA (10^4 nm^2)	Gage length (μm)	E (GPa)[e]	S_y or S_{max} (GPa)[e,f]
1	Fig.2 of [49], 2.1.2a, 2.3.6a	0	V. Low[a]	2.66	5.11	219	7
2	Fig.3 of [49]	0	Intermediate[c]	2.55	8.43	217, 215, 216, 228	1.51, 1.66, 1.70, 2.09
3	2.3.5	9	V. Low	7.11	5.80	216	2.40
4	2.4.2, 2.4.3	9	V. Low	7.31	5.90	225	6.49
5	2.3.1, 2.3.2	9	Low[b]	8.82	7.43	216, 272	1.13, 1.38
6	2.1.2b, 2.3.3, 2.3.4, 2.3.6b	9	Low	9.08	9.20	216	2.57
7	2.3.8, 2.3.9b	9	High[d]	5.49	5.55	216	1.51
8	2.1.2c, 2.2.3b, 2.3.6c, 2.3.7, 2.3.9a	15	High	5.67	8.15	216, 240, 246, NA[g]	1.41, 1.89, 2.31, 1.85

a V. Low is no observable intial dislocations, ~$1x10^8$ nm^{-2}

b Low is ~$1x10^{12}$ m$^{-2,}$ or just a few dislocations and debris loops

c Intermediate is ~$5x10^{13}$ m^{-2}, or many dislocations with debris loops

d High is ~$1x10^{14}$ m^{-2}, and either heavily pre-strained or irradiated

e Sample may have more than one E and S_y depending on if it was a series of tests or not

f S_y is engineering stress at the onset of plastic behavior as indicated by the stress-strain curve, or S_{max} is the highest stress reached if mostly linear

g Fiber 6, Test 4 E not applicable due to bending during loading

2.4.1. Errors in stress

2.4.1.1 Image magnification

Projected width measurements made in the JEOL 3010 TEM in a range of magnifications, 25-200kx, did not directly correlate. Therefore, all image magnification

correlations were calculated and made self-consistent with respect to 100-200kx. This base magnification was chosen as measurements made at 100-200kx in the JEOL 3010 TEM most closely matched those made in the FEI SEM, FEI TitanX, and the I[3]TEM JEOL 2100. (It should be noted that the mechanical test of F5, was performed in a different microscope, the FEI TitanX, with a PI-95 for FEI microscopes.) Had these correlations not been made, the measurements taken at lower magnifications increase the projected widths up to 115%. For F6, the initial projected width measurements at 30kx were 105% larger than when measured at 100kx. Using initial over correlated measurements results in an 11% increase in CSA or a decrease in Young's modulus from 225 to 201 GPa. It is possible there are further errors associated with image magnification. However, for this fiber to reach the calculated E_{100}, a further 26% reduction in image measurements is needed, and up to a 30% reduction for other fibers. A further image magnification error is thus unlikely to be solely responsible for the low fiber moduli.

2.4.1.2 Cross-sectional shape

Projected widths for all fibers were acquired at a tilt range of at least 20°, when limited by the fiber being at one end of the PTP gage section, up to 70° when the fiber was in the middle. The CSA calculation assumes complete fiber symmetry, i.e. that the octahedral edges are 4 equal <110> sides and 4 equal <100> sides. Measurements are made by tilting both directions from the (110) ZA to confirm this, and in the location the fiber failed. However, this is not always possible due to slight variations in fiber thickness or if the fiber fails outside the observable gage section, as was the case with F6, seen in Figure 2.4.3. This fiber fails outside the observable gage section, so CSA measurements are made as close to the failure location as possible. Had the CSA measurement been made at the opposite end of the fiber, the Young's modulus reduces from 225 to 219 GPa, which may explain why this fiber's modulus is anomalously high when compared to the other fibers. It is thus possible to over or under-measure the CSA. However, as stated above, the fiber widths must be ~30% less than measured. As was mentioned in the Johanns, et. al. study, any contamination layer would increase widths measured in the SEM. In the TEM, however, transmission allows the contamination layer to be easily discernable from the fiber, provided the layer is not thick enough to obscure the true fiber edge. Measurements in those areas are easily avoided and the contamination layer thickness did not usually exceed 10 nm. Additionally, misalignment of the fiber, up to 2°, was considered, however, misalignment results in only 0.12% error in measured CSA. Regardless, measurements were made orthogonal to the straining direction. Efforts were made to confirm the true cross-sectional shape of the Mo-alloy nano-fibers and thus unlikely to be solely responsible for the modulus error.

2.4.1.3. Sample load

The actual load seen by the sample is the difference between the load measured by the PI-95 and the load required to displace the PTP. Assuming the measured load is correct and the PTP springs are fully linear in this displacement regime, errors would arise from miscalculation of the PTP load. This occurs when the recorded displacement or measured PTP stiffness are incorrect. Figure 2.4.2b shows the recorded displacement is identical to the DIC measured displacement. To calculate the PTP displacement from DIC true strain, the initial gage length was measured using the SEM and corrected TEM images (see §2.4.1.1 above). Considering a stiffness error of 100 N/m in the PTP springs, the measured Young's modulus changes by only 8

GPa for F6. In fact, even assuming a PTP stiffness of zero will only increase the Young's modulus to 270 GPa. Thus, by assuming measured load is accurate and confirming measured displacement, the measured PTP spring stiffness is also confirmed. As a result, the measured stiffnesses of reused PTP devices show the consistency between tests.

2.4.1.4. Sample misalignment

Misalignment of the single-crystalline Mo-alloy nanofibers would result in a reduction of calculated stress using both geometric[116] and crystallographic arguments. Alignment of the fibers with respect to the PTP displacement axis in both the in-plane and out-of-plane orientations is confirmed in the FIB at the time of sample preparation. However, while loading the PTP in the PI-95 TEM holder, misalignment both in and out-of-plane is possible. The PI-95 holder for the JEOL is designed with two setscrews to affix the copper stub and PTP. The PI-95 holder for the FEI microscopes, used to test F5, has a slightly different stub and end-piece design. The copper stub is affixed with only one setscrew, though the end piece has guide edges. Both holder designs have some play in the stub orientation so initial in-plane alignment is checked with an optical microscope before testing and confirmed in the TEM. Out-of-plane misalignment of the PTP would only occur if the stub was not flush with the holder end piece and this is checked with an optical microscope before the experiment. The indenter motion is monitored during calibration to ensure no in-plane movement. Out-of-plane movement can only be observed through changes in focus, which are rarely obvious, or inconsistencies in measured and observed indenter displacement. It is fortunate these checks are performed at high magnification, usually 200kx, as the systemic image magnification errors of lower magnifications would erroneously indicate a problem. These many checks ensure sample misalignment is not a possible source of error.

2.4.2. Errors in strain

2.4.2.1 Machine compliance

Machine compliance includes the compliance of the load cell and load frame, which occurs if the diamond indenter deforms rather than displaces the PTP, or from compliance of the Crystalbond adhesive used to affix the PTP to the PI-95 holder, to name a few. A 20 µm diameter flat-punch doped-diamond indenter is unlikely to cause material deformation of the Si PTP device. The machine compliance is investigated by comparing the displacement of the PTP gage section, as measured with DIC, to the PI-95 recorded displacement. As stated previously, to calculate the PTP displacement from DIC true strain, the initial gage length was measured using the SEM and corrected TEM images. As seen in Figure 2.4.2b, these two displacement values are identical, indicating any compliance between the machine and PTP is either negligible or accounted for during calibration of the indenter.

2.4.2.2 Pt grip pad compliance

Using the first tensile test of each fiber, no correlation was found between Pt pad volume or pad/fiber contact area to the Young's modulus error. The pad volume of F2 was more than 4x larger than that of F5, yet they have identical modulus errors. The pad/fiber contact area of F4 was almost 3x larger than for F7 again with identical modulus errors. Indeed this was also the case in the Murphy, et.al. study, which also found no correlation to deposition conditions for the same precursor material used here, methylcyclopentadienyl (trimethyl)

platinum. Pt grip pad compliance was investigated by eliminating any effect from the Pt grips by measuring local fiber strain using DIC (Figure 2.4.2). The engineering strain was calculated from the DIC measured true strain and would not be affected by image magnification errors. Although the overall DIC-measured strain is lower, the two strain measurements are identical until 0.64 GPa or 0.28% strain. A similar in-situ TEM tensile study using EBID-Pt grips confirmed tensile strain measurements with corresponding selected area diffraction[117]. The ZnO fibers of the TEM study are of similar size, length, and stiffness to the Si fibers used in the Murphy, et. al. study, but no pad compliance was measured. It is unclear why the TEM results of ZnO nano-fibers and the DIC results of F6 contradict the SEM results by Murphy, et.al. and Johanns, et. al. or through what mechanism the Pt grip pads would fail that would not correlate to their size, contact area, or deposition conditions.

2.4.3. Dislocation effects

2.4.3.1 Dislocation motion outside the gage section

The Pt grips were placed ~1 μm from the PTP edge to reduce the thickness of diffused Pt in the observable gage section (Figure 2.4.4). The tradeoff being a quarter, or more, of the fiber length is unobservable. Though Pt diffusion increases the sample thickness, reducing the likelihood of failure near the grip pad, dislocation motion and plasticity are still possible. For example, F6 has no observable initial dislocations and fails outside the TEM-observable area. The data indicates that, like most intermediately pre-strained fibers, it is likely the fiber had a single packet of dislocations, unfortunately located in this unobserved region. Figure 2.4.2c shows the DIC and PI-95 measured E_{100} are the same up to 0.64 GPa or 0.28% strain, after which the DIC slope increases. By excluding the region that fails, the actual strain of the fiber is seemingly underestimated. Though F6 has no visible dislocations, the dislocation motion for pre-strained Mo-alloy nanofibers begins around the bulk yield strength, 300-650 MPa. By increasing the assumed elastic stress-strain data of F6 from 0.64 to 1.2 GPa, the DIC measured Young's modulus increases to 265 GPa. This demonstrates the possibility of overestimating the Young's modulus by including data after the yield point, and the importance of TEM observation during testing.

2.4.3.2 Easily mechanically-annealed defects

The Cu tensile samples of the Kiener and Minor study were shaped with the FIB, creating ion beam damage near the surface. This damage is often easily mechanically or thermally annealed and has been shown to reduce flow stress for many materials in nano-compression experiments. For example, a study by Lowry, et. al. compares the compressive mechanical behavior of FIB-shaped Mo pillars with and without thermal annealing[37]. Thermal annealing is shown to fully eliminate the FIB damage, resulting in pristine pillars that achieve ideal strength and increase measured Young's modulus from 50 to 100 GPa. Though nano-indentation of FIB-irradiated Mo-(3at.%)Nb surfaces found no change in modulus [31], the discrepancy is likely due to the shape. FIB defects are easily annealed at the surface of nano-pillars, but do not escape easily during nano-indentation. Figure 2.4.1b shows the measured Young's modulus of all tensile tests the fibers presented in this chapter underwent as a function of the fiber's initial dislocation density. The measured elastic modulus for F3, with a low initial dislocation density, shows an increase from 216 to 272 GPa after the first test reduces the

mobile dislocation density by half. E_{100} of the heavily dislocated fiber, F8, increases from 216 to 240 GPa after the first test, and to 246 GPa after the second. Presumably, this fiber has many dislocations that are close to the surface that can easily annihilate. The effect is not as pronounced as for the low dislocation density fiber due to the many dislocations impeding dislocation motion. F2 has several packets of dislocations throughout for a mid-range dislocation density, and subsequent testing only increases E_{100} from 216 to 228 GPa. The fiber has too many mobile dislocations to appreciably reduce their density, but not enough to impede their motion. It is interesting the subsequent tensile tests produce moduli that follow the generalized size-dependent Taylor-strengthening law[61,118], indicating the lower modulus may be defect mobility driven.
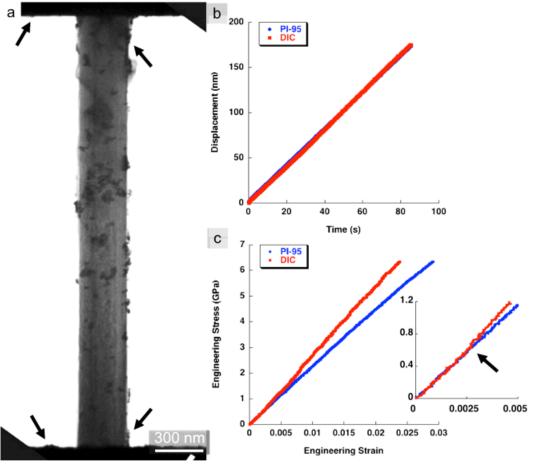
Figure 2.4.2: (a) TEM micrograph of Mo-alloy nano-fiber decorated with gold nano-particles. Black arrows to the left of the fiber indicate where DIC was used to track the actual displacement of the PTP gage section. Black arrows to the right of the fiber indicate where DIC was used to track the actual displacement of the fiber. (b) Displacement vs. time graph comparing the displacement of the PTP as measured with the PI-95 and DIC. The identical loading curves indicate no compliance between the PI-95 and the PTP. (c) Engineering stress vs. engineering strain loading curves comparing the PI-95 measured strain against that of DIC. (inset) Shows the two curves deviate at 0.64 GPa or 0.28% strain. This is likely due to the fiber deforming outside the observable gage section rather than compliance of the Pt grips.
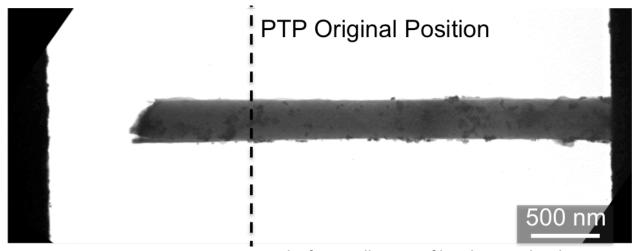
Figure 2.4.3: Post-mortem TEM micrograph of a Mo-alloy nano-fiber decorated with Au nano-particles. This fiber failed outside the observable gage section, as indicated by the dashed line.
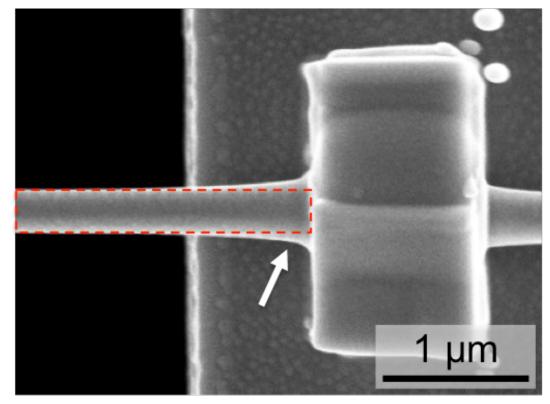
Figure 2.4.4: SEM micrograph of Mo-alloy nanofiber attached to PTP with Pt grip pad. The dashed lines indicate the true dimensions of the fiber. The white arrow indicates where the thickness has increased due to Pt diffusion.

2.5 Summary and conclusions

Quantitative in-situ TEM tensile tests of Mo-alloy nano-fibers were performed for three purposes. This first is to investigate the feasibility of experimentally measuring defect interactions with high enough load and displacement resolution to directly compare to computational simulations. This was investigated by measuring local true stress around a Frank-Read source activation, with results that compare remarkably well, ~1% differences, to predicted values using a simple line tension model. The implications of such high-resolution quantitative measurements are numerous, not the least of which is direct comparison to computation models. The second purpose was to explore the feasibility of experimentally measuring defect interactions with a high enough temporal resolution to capture deformation mechanisms at high stresses. This was evaluated through the attempt to capture the mechanism responsible for the sudden, large strain bursts seen in dislocation exhausted and starved Mo-alloy nano-fibers using two different in-situ TEM cameras. Unfortunately, despite using state-of-the-art imaging technology with the Gatan K2 direct electron detector camera, which increases the probe rate from 30 fps to 400 fps, the dislocation multiplication processes are still too fast to be captured. The last purpose was to analyze the effects irradiation-induced microstructural changes have on the deformation mechanisms responsible for mechanical behavior. The results show that collective defect behavior, regardless of defect type, can lead to similar mechanical properties. Thus, to probe fundamental behavior, detailed analysis of the initial, transitional, and final dislocation structures of irradiated specimens, perhaps by using 4D electron tomography, is needed.

Chapter 3: FCC Gold Thin-Films

Gold was chosen as a model FCC material system as it has no native oxide, ensuring optimal imaging conditions in a wide range of thicknesses, and low stacking fault energy, which ensures adequate radiation-induced defect production, or high cascade efficiency. Radiation-induced defects include stacking fault tetrahedra (SFTs) and other vacancy clusters, and gas-filled cavities resulting from neutron-alpha particle reactions. SFT and dislocation interactions are of particular interest in understanding the mechanisms of radiation-induced hardening of neutron-irradiated FCC metals[119], and helium embrittlement at higher temperatures must be understood for the development of new reactor structural materials[120]. Additionally, the most prevalent irradiation-induced defects of nano-scale mechanical testing are due to FIB irradiation, as many researchers take advantage of the widely applicable nature of the sample preparation tool. Presented here are studies that focus on the experimental hurdles that must still be overcome in order to understand defect interactions in FCC materials at a fundamental level. They include the application of two novelly-applied strain mapping techniques that pave the way for 4D in-situ TEM experiments (§3.3.1), and investigations of irradiation-induced microstructural evolution in FCC materials that affect the deformation mechanisms responsible for mechanical properties and behavior (§3.3.2).

3.1 Au thin-film sample preparation

3.1.1 Physical vapor deposition and annealing

Gold thin-film was evaporated from 60mg of 99.99% purity Alfa Aesar gold foil in a tungsten boat onto a freshly cleaved sodium chloride (NaCl) substrate at 150°C. The contamination level and grain size of the film was optimized by maintaining a pressure of $6x10^{-5}$ Pa during deposition, then remaining at temperature for 4 hours under vacuum. TEM samples were prepared by dissolving the NaCl substrate in deionized water then floating the thin film onto a standard copper TEM grid. Scanning electron microscopy (SEM) was used to confirm the thickness of the film. A layer of protective Pt was first e-beam deposited onto the film, then a 30keV Ga ion beam was used to cross-section the Pt-Au-Copper grid layers (Figure 3.1.1). The Au thin-film was measured to be ~100 nm before and after the annealing described below.

To make FIB-free tensile samples from thin-films, an additional annealing step was used to create holey films from the as-grown continuous film. The holes serve as the edges of the traditional dog-bone shape of tensile samples, ensuring no FIB damage in the tensile gage section. The additional annealing process involves vacuum annealing the thin-film for 4 hours on the NaCl substrate at 300°C, above the sub-grain coalescence temperature of Au of 262°C [121], and well below the melting temperature of NaCl, 800°C [122]. This results in a holey microstructure with many ligands around 100 nm in width, as seen in Figure 3.1.2.
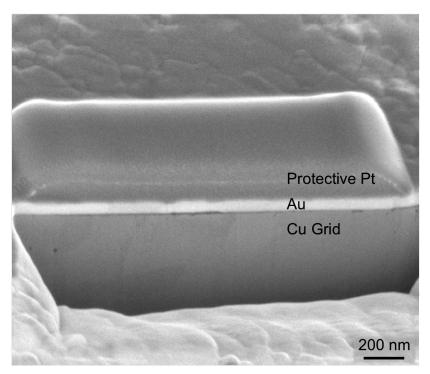
Figure 3.1.1: SEM micrograph of Au thin-film thickness cross-section at a sample tilt of 45°.
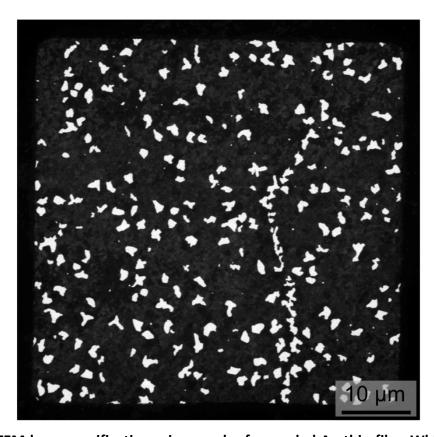

Figure 3.1.2: TEM low-magnification micrograph of annealed Au thin-film. White areas show the holes formed by the annealing process.

3.1.2 He[1+] ion implantation and bubble growth

In-situ ion irradiation was performed at the I³TEM at Sandia National Laboratories' Ion Beam Lab[70]. A 10keV He[1+] ion beam was introduced into a JEOL 2100 TEM, operating at 200 keV, along a nominally orthogonal path to the electron beam, and 30° to the sample (See Figure 2.1.3 from §2.1.4). Unlike typical ion irradiation of bulk samples, the ion beam energy was not varied so as to homogenously implant He[1+], as the I³TEM did not yet have the capability to continuously vary the ion beam energy. Therefore, a 10keV He[1+] beam was chosen to maximize the helium concentration near the mid-plane of the thin film and thus minimize surface effects. He[1+] was implanted at a dose rate of 3.8×10^{13} ions cm^{-2} s^{-1} and taken to a total dose of 1.6×10^{17} ions cm^{-2}. The damage-thickness profile per ion (Figure 3.1.3) and sputter at both entry and exit surfaces were calculated for He[1+] using the Transport of Ions in Matter (TRIM) monolayer calculation with a 30° incident angle and a layer thickness of 100 nm[71]. The number of sputtered atoms throughout the experiment was found to be negligible by SRIM simulation and was therefore assumed to play no role in the experimental observations. These calculations show a maximum dose of 33 dpa at 10 nm from the incident surface, with the majority of He ions reaching a 35 nm implantation depth.

The film was then annealed in-situ in the TEM to grow the helium bubbles to an easily observable size, but before reaching the critical void size. This is achieved by ramping to 633K (T=0.47T$_m$) and holding for 15 minutes. Annealing quickly heals the displacement damage, seen in Figure 3.1.4b as small defect clusters and loops and larger dislocations. The resulting microstructure is shown in Figure 3.1.4c. The Fresnel contrast of the bubbles below focus shows a relatively even distribution throughout the film, with some segregation of He bubbles at grain boundaries.
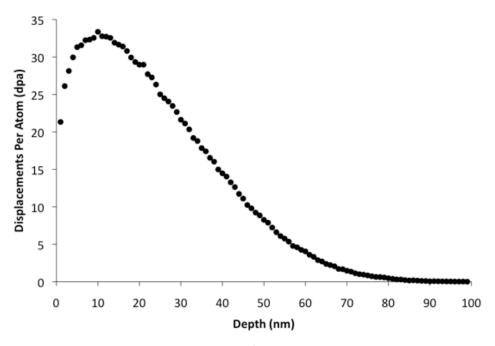

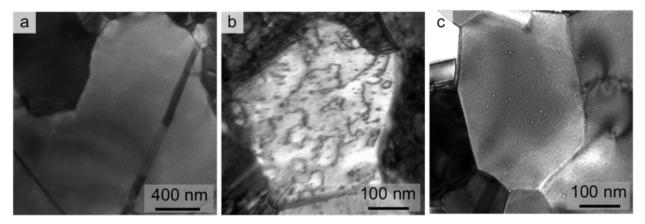**Figure 3.1.3: Depth damage profile of 10 keV He[1+] irradiation of Au.**

Figure 3.1.4: TEM bright-field micrographs of Au thin film (a) unirradiated, (b) He[1+] irradiated, and (c) after in-situ heating of irradiated Au thin-film. Underfocused image shows He bubbles as small white dots. Image modified from [123].

3.2 Experimental methods

To quantitatively study unit defect interactions with high enough spatial resolution and strain precision, electron microscopy is the obvious choice, and a recent review[46] of electron microscopy strain mapping shows no shortage of techniques available, each with their own advantages and drawbacks. Of particular interest, due to their wide fields of view and nanometer resolutions, are electron holography and nano-beam electron diffraction (NBED). Holography is usually achieved with off-axis setups[47], however these require an electron bi-prism, which is difficult to achieve experimentally[124]. To bypass this experimental barrier, an in-line dark-field holography (DFIH) setup was developed[125]. Though initially applied to semiconductors, here the applicability of DFIH to metals is investigated. Additionally, major technological advances in imaging and computational technology have vastly improved the use of NBED, as presented here. Both demonstrate the feasibility of 4D strain mapping[126] to be used (§3.3.1), for example, during in-situ TEM mechanical tests of unirradiated and irradiated Au thin-films (§3.3.2), to map strain as a function of time.

3.2.1 Dark-field Inline Electron Holography

Dark-field inline electron holography (DFIH) was developed to map strain by directly measuring the phase of diffracted beams [127]. The phase of the diffracted beam is related to the strain along with other factors such as the specimen thickness, through the mean-inner potential of the material, and dynamic scattering. By capturing the phase of two non-collinear diffracted beams, the two-dimensional strain tensor can be precisely determined. The setup for DFIH is similar to conventional off-axis electron holography except that the experiment is carried out in dark-field mode, i.e. that the diffracted beam is oriented along the optic axis by tilting the incident beam, but with more relaxed requirements on the spatial coherence of the electron beam[125]. A part of the diffracted beam emerging from an unstrained part of the specimen, in this case away from visible defects, is interfered with the beam emerging from the region of interest, and for a given specimen thickness and diffraction condition, the resulting phase difference is due only to strain. With DFIH, a much larger area can be mapped as

compared to high-resolution strain mapping techniques such as peak-finding[128] or geometric phase analysis (GPA)[129]. This makes DFIH particularly attractive as a technique that could be combined with in-situ TEM mechanical deformation studies, since large fields of view can be mapped and the only additional capabilities required are the imaging of a focal series. The technique of DIH can be pushed to a spatial resolution of 1 nm[130] and the precision can reach 2.10-4 in strain profiles if lateral averaging is applied[131].

DFIH was used to map the strain distribution around a He bubble implanted in a Au thin-film using an in-column Omega energy-filtered Zeiss Libra TEM operating at 200keV, with a 10 μm objective aperture for a 0.8 nm spatial resolution. A dark-field focal series using a [111] diffracting vector consisting was recorded with a step size of 2 μm. The Full-Resolution Wave Reconstruction (FRWR) algorithm software was used to calculate the strain field from the dark-field focus series[132].

3.2.2 Nano-beam Electron Diffraction

Nano-beam electron diffraction (NBED) is, as the name implies, a diffraction-based technique that can be used to measure strain with high strain precision at nanometer spatial resolution. This is achieved with a quasi-parallel electron beam with a diameter at full-width at half-maximum on the order of a few nanometers, and convergence angle of only a few milliradians. With such a nano-beam, lattice strain is probed only in the beam width from the acquired diffraction pattern (DP). Then, by rastering the beam, a strain map can be made; the resolution of which is dependent on the beam size, step size, and beam broadening through the sample. Figure 3.2.1 shows a schematic of the technique used to acquire a strain map. The full-view of the area to be mapped is shown on top, with a few representative DPs taken at individual pixels shown below. The collective stack of DPs is then analyzed for lattice strain along a specific direction, and the above image is re-plotted with the calculated lattice strain values (see, for example, Figure 3.3.2).

Though not a new technique, nano-beam electron diffraction for strain mapping has recently become feasible due to advances in both imaging technology, and data processing and storage. The Gatan K2-IS direct electron detector camera (see also §2.3.2) allows for orders of magnitude increases in frame rate, up to 1600 fps, which can lower the acquisition rate of a large map, 128x256 pixels, to less than a minute. For comparison, at the usual 30 fps the same size map would take over 18 minutes to acquire. This is important for many reasons, not the least of which is a reduction in drift effects. Additionally, the ever increasing data storage limit allows for the acquisition and storage of the ~30k images needed for nano-beam diffraction strain mapping. And since the location of the K2 camera along the beam path allows for simultaneous detection by a High-Angle Annular Dark-Field (HAADF) detector, concurrent strain mapping and sample observation during in-situ TEM testing is feasible.
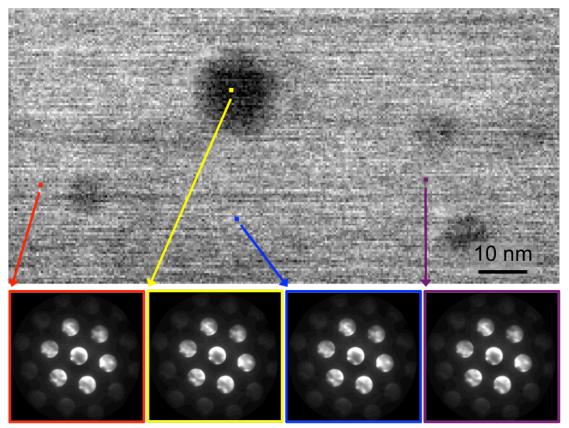
Figure 3.2.1: Schematic of images acquired for NBED. Top image is a co-obtained HAADF image of four bubbles in Au thin-film. Lower images are representative DPs taken at individual pixels in the 128x256 pixel image.

NBED was carried out on the TEAM I instrument at the National Center for Electron Microscopy at LBNL, whose three independent condenser lenses allow the formation of a sub-nanometer electron probe with a semi-convergence angle of 1.5 mrad, using a 40 μm condenser aperture at 300 keV. Convergence angle is optimized for brightness and nearly touching disks, as shown in the representative DPs in Figure 3.2.1. The microscope was set up in Scanning Transmission Electron Microscopy (STEM) mode, and during simultaneous acquisition of the HAADF image (256x128 pixel), a DP was acquired for every pixel position by the Gatan K2-IS direct electron detector camera operating at 400 fps. The strain map was calculated from the resulting data cube consisting of ~33000 nano-beam DPs using custom scripts[133] implemented in DigitalMicrograph. The positions of the diffracted peaks are deduced for each DP by cross correlation with an artificial mask, constructed to fit the size and shape of the spots. A reference was defined in the unstrained gold thin-film and for each DP the transformation matrix between the unstrained DP and the DP was calculated. Strain and rotation matrices were deduced from the transformation matrix using polar decomposition.

3.2.3 In-situ Mechanical Testing

Tensile specimens of Au thin-films were prepared one of two ways. The first uses FIB to shape the sample. A small piece of film is floated onto the PTP, as shown in Figure 3.2.2. The PTP is affixed to a copper mounting stub with Crystalbond polymer adhesive, and placed in the

dual-beam SEM/FIB. The FIB is then used to cut film away from the moving parts of the PTP device, and finally to shape the sample (Figure 3.2.3). The final shaping step is done using blind FIB cuts such that th e gage section of the sample is never imaged, and the only FIB damage is at the shaped edges.

The second method is similar to that used in preparing nano-fiber tensile samples (§2.2.2). Free-standing film is prepared by floating a small piece onto a standard copper TEM grid. For holey film, first an appropriate area is selected. Criteria include two holes about 100 nm apart such that the ligand between them is a dog-bone shape, and no holes at least 5µm above where the tensile sample will be, as seen in Figure 3.2.4b. This is to ensure no stress concentrations in the film aside from the intended gage section. After an appropriate area has been found, e-beam deposited Pt (EBID-Pt) is laid in four thin support strips (Figure 3.2.4a). Then three blind FIB cuts are made, leaving the end opposite the nano-manipulator still attached (Figure 3.2.4b). After the nano-manipulator is attached to one end of the sample with EBID-Pt, a last blind FIB cut is made to free the sample. It is then transferred and attached to the PTP device using EBID-Pt. Finally, the side supports are cut away using small, blind FIB cuts, made quickly and carefully to avoid redeposition and exposure to the ion beam (Figure 3.2.4d). Tensile testing is then carried out per the method described in §2.2.
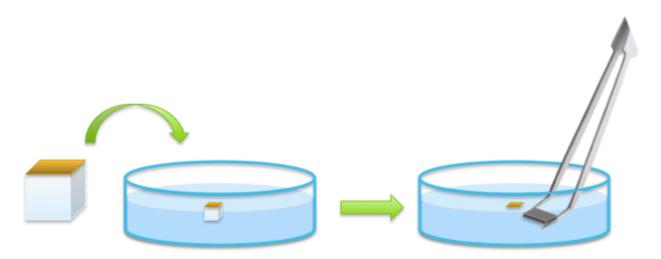
Figure 3.2.2: Schematic of thin-film floating technique. A small piece of Au thin-film on the NaCl substrate, ~1x1 mm², is placed into a Petri dish of DI water. It will float on the surface as the NaCl dissolves and remain on the surface, provided it is handled delicately. The PTP is then maneuvered underneath the floating film with tweezers. The PTP is then carefully raised such that the film is laid over the gage section of the device.
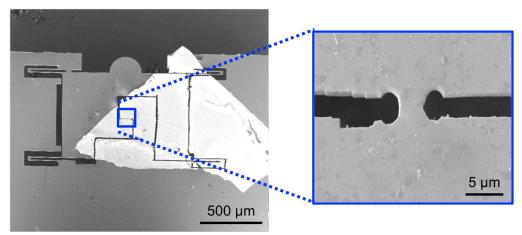
Figure 3.2.3 SEM micrographs. Left image shows PTP with floated Au thin-film. FIB cuts are made to clear the film away from all moving parts. The zoomed-in image shows the final tensile sample. All FIB cuts in this region have been made blind to minimize FIB exposure damage.
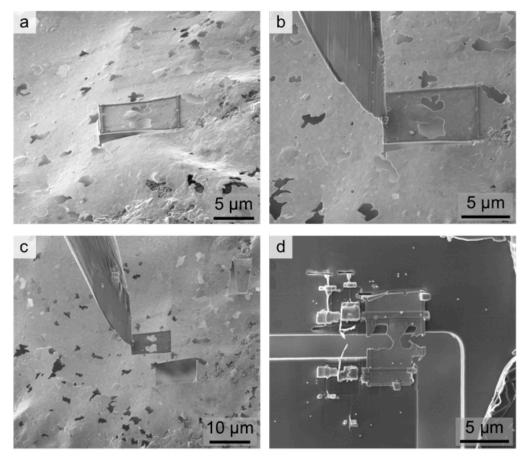
Figure 3.2.4 SEM micrographs of thin-film tensile sample preparation. (a) 4 Pt support strips are laid down using e-beam deposition and three sides cut using blind FIB cuts. (b) Nano-manipulator is attached using e-beam deposition to the freed end of the sample. (c) The last edge is cut using a blind FIB cut. (d) The sample is transferred to the PTP device and attached using e-beam deposited Pt. The side supports are then cut away using blind FIB cuts.

3.3 Results and discussion

3.3.1 Strain mapping irradiation defects

Alpha particles, or helium, are created in some materials during irradiation from neutron-induced transmutation, particularly in the FCC austenitic steels used in reactor pressure vessels[134], and it is well known that helium bubbles affect mechanical properties[135]. For example, bubbles are shown to be strong obstacles to dislocations in simulations[21], and cause dimensional instability, or swelling, once they grow into voids, which are un-pressurized cavities. This neutron-irradiation-induced process can be experimentally simulated through helium ion implantation. Helium is highly insoluble in metals, and helium bubbles, which are pressurized cavities of helium, will nucleate at a vacancy cluster[136]. Experimentally, bubble properties have been determined using several methods[137], among them geometric derivations using irradiation parameters (referred to henceforth as the geometric method or GM). This is done with helium ion implantation experiments by first assuming all helium has diffused to a cluster, and then estimating the number of bubbles and their size to gain a total volume. Thus, an approximate helium density can be calculated from the number of helium ions implanted. Alternatively, spectroscopic techniques, such as Electron Energy Loss Spectroscopy (EELS) can be used [138–142]. In a method developed by Walsh, et al. [138] EELS is used to measure the He density directly from the electron energy-loss signal. The appropriate equation of state must then be used to calculate the pressure in the bubbles from the He density. Both techniques yield the He density in the bubbles, though neither directly measures the strain field created by the bubbles. Experimental investigations of bubble-filled microstructures often use simplified correlations between size and pressure of the bubble to estimate the mechanical properties. Presented here is an interesting case study regarding the microstructural change of helium bubbles in irradiated Au thin-film, and more details can be found elsewhere[123].

3.3.1.1 Dark-field inline holography results

Free-standing irradiated gold thin-film is prepared using the methods outlined in §3.1. Dark-Field Inline Holography (DFIH) is performed per the method outlined in §3.2.1. Figure 3.3.1 shows a strain map of a single He bubble in the Au thin-film measured using DFIH. The Au thin-film is tilted to a [110] zone axis, and a combined dark-field focal series (Figure 3.3.1a) using a [111] diffracting vector is used to determine a quantitative strain map (Figure 3.3.1b). The bubble has a symmetric peak compressive strain of 0.67%. Note that the strain field of the bubble is radially symmetric, such that the strain ε_{xx} appears negative on one side and positive on the other.
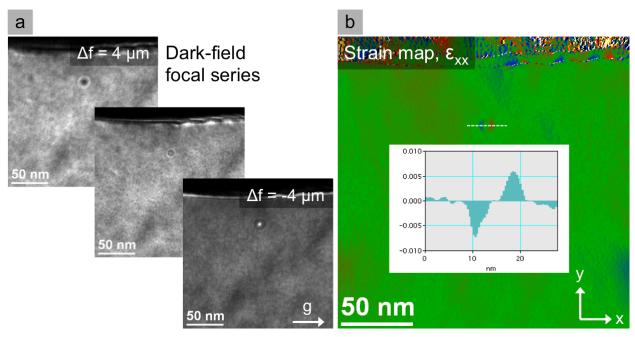
Figure 3.3.1: (a) Dark-field focal series of single He bubble in Au thin-film. (b) Resulting ε_{xx} strain map of bubble determined through dark-field inline holography with inset strain profile. The strain field of the bubble is radially symmetric, so the strain will appear negative on one side and positive on the other. From [123].

3.3.1.2 Nano-beam electron diffraction results

Nano-Beam Electron Diffraction (NBED) on the same irradiated free-standing Au thin-film used for DFIH, and performed per §3.2.2. Acquisition times were greatly reduced to ~80s by using the Gatan K2 camera operating at 400 fps. Figure 3.3.2a shows a co-obtained HAADF-STEM image revealing the presence of multiple bubbles in the acquisition window. For every pixel position a nano-beam diffraction pattern was acquired. The summed diffraction pattern is shown in Figure 3.3.2f, showing a [111] zone axis oriented Au grain. Figure 3.3.2b-e shows the color-coded strain map calculated from the nano-beam diffraction patterns for different orientations. A compressive strain is revealed at the interface of the bubble, with a maximum magnitude of 0.7%.
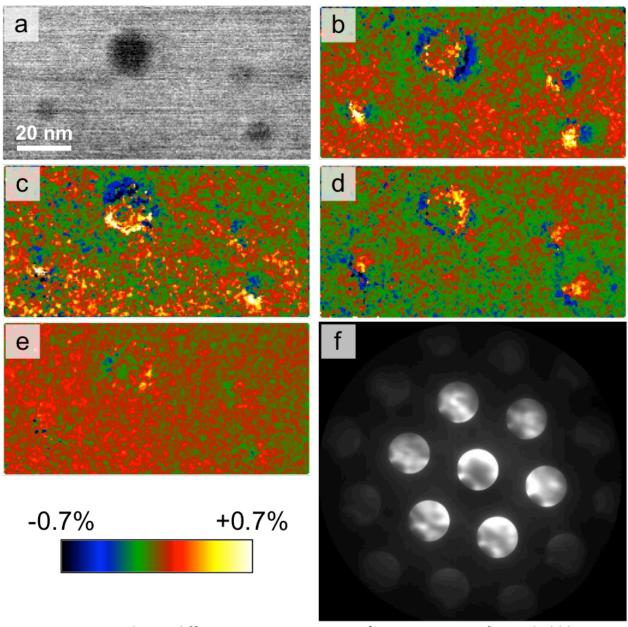
Figure 3.3.2: Nano-beam diffraction strain mapping. a) HAADF image of 4 He bubbles in Au thin-film. b) ε_{xx} c) ε_{yy} d) ε_{xy} e) rotation f) representative mean diffraction pattern. From [123].

3.3.1.3 Discussion of transmission electron microscopy strain mapping

The similar sizes and measured strains of the two electron microscopy strain mapping techniques allow for direct comparisons using a single bubble. Used here is the large, 12 nm diameter, bubble in Figure 3.3.2. The internal pressure of a gas-filled cavity is

$$P = \frac{2\gamma}{R} + \sigma_r$$

(3.3.1)

where the first term is the Kelvin relation[143,144] for a cavity of radius R whose internal pressure is in mechanical equilibrium with its surface tension, γ=1.17 N/m for Au at room temperature[137]. The second term σ_r is an all-encompassing term that represents any mechanical stress at the cavity surface, and is equal to zero when the cavity is in mechanical equilibrium with the surrounding matrix material. The annealing step, 633K for 15 minutes to grow the helium cavities, was performed in-situ in the TEM. Thus, through direct observation, the maximum internal cavity pressure can be estimated, as the cavity pressure must be below the dislocation loop punching (LP) pressure, as other athermal mechanisms such as self-interstitial creation or inter-bubble fracture or blistering, require higher internal pressures. Dislocation loop punching is an athermal process whereby cavities relieve internal pressure and grow through the creation of dislocation loops around the cavity. No loop formation was observed during the anneal, the quench, or after. As such, it is likely the internal cavity pressure is still below the LP pressure in the room-temperature strain mapping experiments. The upper limit for the internal pressure of the cavity is then

$$P_{LP} = \frac{2\gamma}{R} + \frac{\mu b}{R}$$

(3.3.2)

where μ=27 GPa is the isotropic shear modulus, and b=.2883 nm is the magnitude of the Burgers vector. This neglects any energy barriers, and holds true for 2<R/b<10, with the full expression dependent on the dislocation configuration, as discussed in Ch.2. As the 12 nm bubble here would result in dislocation loops larger than R/b=10, the second term will be taken as the extra pressure to create a larger prismatic loop, with the result[137]

$$P_{PLP} = \frac{2\gamma}{R} + \frac{\mu b}{2\pi R_L (1-v)} \ln\left(\frac{R_L}{r_o}\right) = 1.5 GPa$$

(3.3.3)

where R_L is the radius of the nucleated dislocation loop, taken to be equal to R in this case, v=.43 is the Poisson's ratio, and r_o is the core radius and taken to be equal to b. The maximum strain at the cavity surface is then ε=σ_r/μ=4.1%, which is reasonable[145]. Using then the ideal gas law and the maximum pressure calculated in eq. 3.3.3 the maximum vacancy to helium ion ratio, or helium density, in the 12nm diameter bubble can be calculated as 1V:6He. Note this means a maximum of only 10.58% of the implanted helium is present in bubbles, using an average bubble to film volume ratio of ~0.4% (Figure 3.1.4c), thus without an accurate measure of the number and size of vacancy/gas clusters, a geometric method approximation would result in high errors.

Due to volume interactions, the strain at the bubble interface could be higher than the 0.7% that was measured using the DIH and NBED strain mapping techniques. Thus, a minimum

internal bubble pressure can be found using the strain mapping data. By setting $\sigma_r=.007\mu$ in eq. 3.3.1, the minimum internal pressure is calculated as P=579 MPa, which corresponds again, by using the ideal gas law, to a minimum helium density of 1V:2.4He.

Further defect characterization is needed to show the accuracy of the presented advanced electron microscopy strain mapping techniques, for example, by analyzing different He implantation and annealing conditions. However, the results demonstrate the feasibility of adopting 4D strain mapping during in-situ TEM testing to directly quantify strain fields around individual defects. A particularly important implication of directly measuring strain is the equation of state of these high-pressure cavities does not need to be known. This removes the reliance on empirical equations of state, and moves computational methods towards to a more fundamental understanding of the processes dictating mechanical properties and behavior.

3.3.2 Mechanical testing of unirradiated and irradiated Au thin-film

The role of helium and other irradiation-induced defects in mechanical property evolution and degradation remains an outstanding issue. Computational studies have modeled dislocation interactions with bubbles, stacking fault tetrahedra, faulted loops, etc., however no experiments have quantitatively probed these interactions to date. This section presents a step towards this goal. As in the testing of Mo-alloy nanofibers (Ch.2), presented here are the collective defect behavior of edge-localized Ga^{3+} FIB-shaped, He^{1+} implanted, and their combined effects, as compared to unirradiated, FIB-free Au thin-film. Where possible, the engineering stress-strain data, the tensile loading crystallographic direction, and the measured and calculated Young's moduli are presented.

3.3.2.1 Unirradiated FIB-free (UFF)

Unirradiated holey Au thin-film was prepared following the procedure outlined in §3.1 and §3.2.3, and loaded in uniaxial tension according to §2.2.1. Figure 3.1.2 shows the ligand between holes, or the gage section, is a single grain with tensile loading direction near <123>. The surface contamination layer was examined with selected area electron diffraction (SAED) and found to be primarily redeposited gold in an amorphous carbon matrix, likely forming during the initial freeing from the film (Figure 3.2.4a,c) and/or the final cutting of the edge supports (Figure 3.2.4d). In-situ video of the mechanical test was recorded at 30 fps, and the mechanical data was determined with DIC measured strain. Interestingly, a sudden strain-softening event occurs at 5.6% strain, or t=90.00s (Figure 3.3.3b-c), resulting in an 8.3% increase in strain in $1/30^{th}$ second. The sample continues to neck in this region and deforms plastically for a total elongation reaching 27.3% (Figure 3.3.3d). The fracture surface shows ductile transgranular fracture, with typical ductile cup-cone geometry, indicating multiple active slip systems.
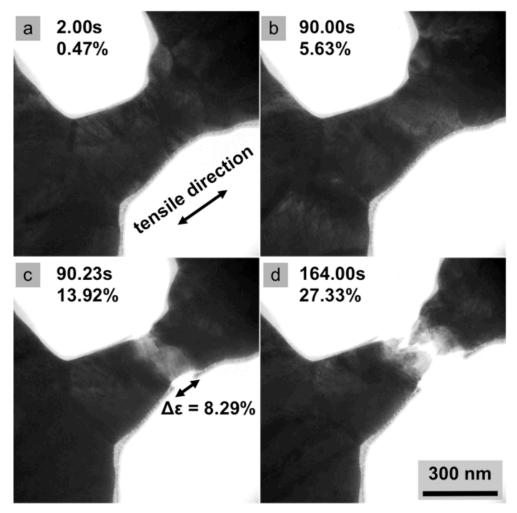
Figure 3.3.3: Still frame images from an in-situ TEM tensile test of FIB-free, unirradiated, holey Au thin-film. (a) Initial microstructure. The black arrow indicates the tensile direction of this and subsequent tests. (b) Frame before a sudden strain event, which occurs in less than 1/30th second. (c) After the strain event. (d) Frame before failure.

3.3.2.2 Unirradiated FIB-shaped (UFS)

Unirradiated continuous Au thin-film was prepared following the film-floating then FIB-shaping procedure outlined in §3.2.3, and loaded in tension according to §2.2.1. Figure 3.3.4 shows the stress-strain curve and corresponding microstructure. The sample is loaded fairly elastically, with some unbending, until it reaches an ultimate tensile strength of 310 MPa and begins to plastically deform. The thin-film has significantly thinned in the middle of the gage section by 5% strain (Figure 3.3.4c). A small crack has begun to form by 6% strain at a triple junction (Figure 3.3.4d) and propagates transgranularly until 8.8% strain (Figure 3.3.4e), when it quickly propagates through nearly the full width of the sample (Figure 3.3.4). The crack is arrested before reaching the edge, leaving a small portion attached, requiring further loading until it fails at 9.5% strain (Figure 3.3.4g). The primary failure grain is oriented with a tensile direction of <-113>, with resulting highest Schmid factor (m=.44) slip systems of [-101](-1-11) and [011](111). The measured Young's modulus is 20 GPa, which is much lower than the expected anisotropic modulus E_{113}= 61 GPa[103,105,106,146,147]. This discrepancy could be due to

concurrent de-buckling of the sample in the elastic loading regime, or if the film thickness is actually much thinner than the assumed 100 nm.
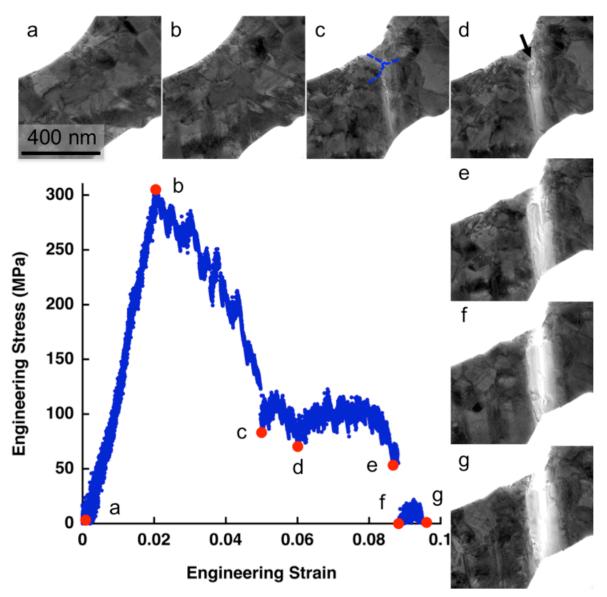
Figure 3.3.4: in-situ TEM tensile test of FIB-shaped, He1+ irradiated Au thin-film. (a) σ= 0. Initial microstructure. (b) σ=310 MPa After the first large load drop. At this point the sample begins to thin noticeably in a band 60° to the loading direction. (c) σ=84 MPa The sample has begun to thin 60° from the loading direction. Overlaid in blue dashed lines is the triple junction where a crack will form. (d) σ=71 MPa A crack has formed in the sample at a triple junction (black arrow). (e) σ=54 MPa The frame before the crack propagates transgranularly across most of the sample. (f) σ=0 GPa. The sample fully unloads as the crack propagates through nearly the full width of the sample. (g) σ=0 GPa. Final microstructure.

3.3.2.3 Irradiated FIB-free (IFF)

Two FIB-free, He^{1+} implanted samples are presented here, with different initial defect structures. Both have a grain boundary in the middle of the gage section, but the first is oriented with the primary grain loaded along the <014>, and the second along the <314>. Additionally, the first sample has no visible He^{1+} cavities, while the second does. The resulting mechanical behavior demonstrates the effect anisotropy and initial microstructure can have.

The first sample, IFF1 (Figure 3.3.5), has no obvious cavities, and a grain boundary orthogonal to the tensile direction at the minimum CSA point. The thin-film deforms fairly elastically, until 4.33 GPa, when yielding is accompanied by plastic instability, similar to the UFS sample above. This behavior is also seen in neutron-irradiated samples[102], where the yield point increases with dose while the plastic instability point remains constant. In a similar manner to the UFS sample, localized deformation can be seen near the sample edge, appearing to crack. However, the crack does not propagate and instead the material glides easily. Surprisingly, the sample does not fail at the grain boundary, and instead transgranular slip is initiated at or near a {111} twin boundary, with the deformation geometry appearing very cup-cone-like. Unfortunately, the sample surpassed the expected total elongation and was therefore not taken to failure. The tensile direction of the primarily deformed grain is near <041>, and the adjacent grain was loaded along <101>. If the calculated anisotropic elastic modulus is taken as the average modulus in the two grains, $E_{041/101}$=65 GPa[103,105,106,146,147], then the measured modulus, 63 GPa, compares nicely.

The second He^{1+} irradiated sample, IFF2 was taken from an area less than 100 µm from IFF1, so that variations in beam intensity and film thickness between the two samples are minimized. IFF2 (Figure 3.3.6), is similar to the first in that it has a grain boundary at the minimum CSA point oriented orthogonally to the loading direction. However, visible bubbles are observed in this sample near a twin (Figure 3.3.6a), ~400 nm away from the gage grain boundary. It is possible there are bubbles closer to the gage section as their size ranges from 4-10 nm and could be obscured by other damage in the 100 nm thick film, but none were directly observed. The grains on either side of the gage grain boundary are both <111> oriented with a 28° rotation between the two. The tensile direction is then about +14° from [-101] in the left grain and -14° in the right, or a mutual <134> tensile direction. The sample loads fairly elastically until 1 GPa or 1.2% strain, though dislocation motion began at 0.27 GPa (Figure Xc). In the elastic regime, the measured and calculated anisotropic Young's moduli are 84 and 82 GPa[103,105,106,146,147], respectively, or a 2% difference. At the ultimate tensile strength of 1.12 GPa, a crack has formed at the edge of the sample at the grain boundary. It grows slightly before fully propagating along the grain boundary at 1.07 GPa, for a brittle intergranular failure.
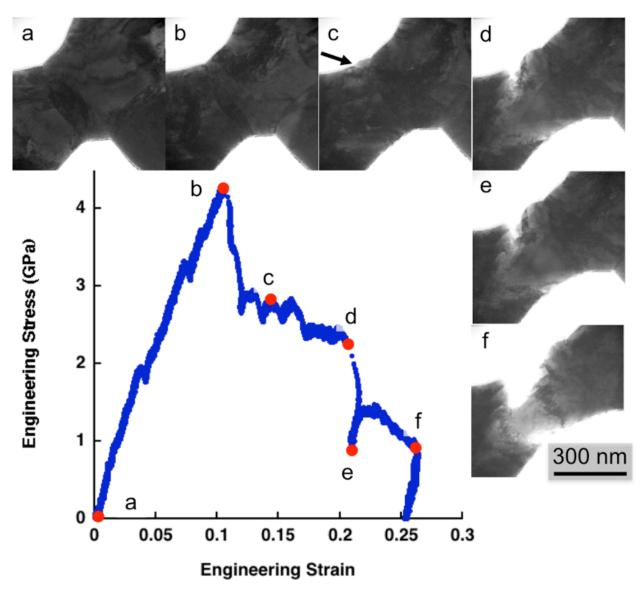
Figure 3.3.5: IFF1: In-situ TEM tensile test of He[1+] irradiated, FIB-free, holey Au thin-film. (a-e) Still frames from in-situ TEM video. Loading direction of the primarily deformed grain is (a) σ=0. (b) Maximum tensile stress reached is 4.33 GPa. Slip is localized on or near a twin boundary. (c) A crack forms (black arrow) at σ= 2.87 GPa. (d) Frame before easy glide at σ= 2.24 GPa. (e) At the end of easy glide, σ= 0.89 GPa. (f) Frame before the sample begins to unload at σ= 0.84 GPa. The sample was not taken to failure.
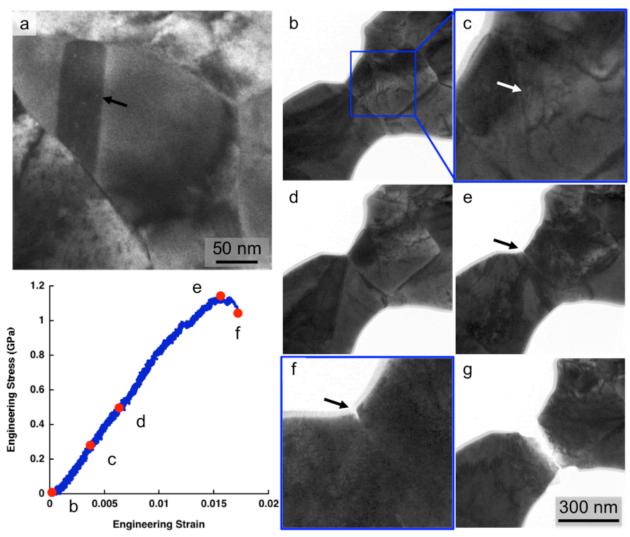
Figure 3.3.6: IFF2: In-situ TEM tensile test of He[1+] irradiated, FIB-free, holey Au thin-film. (a) TEM micrograph of an area ~400nm away from gage area. Black arrow indicates several cavities near a twin. (b-g) Still frames from in-situ TEM video. (b) σ=0. (c) Magnified and cropped frame showing the first observation of dislocation motion from a spiral source (white arrow) σ=0.27 GPa. (d) First large collective dislocation motion σ=0.51 GPa. (e) Crack initiates (black arrow) σ=1.12 GPa. (f) Magnified and cropped last frame before failure σ=1.07 GPa. (g) Sample after failure.

3.3.2.4 Irradiated FIB-shaped (IFS)

From a continuous region of the same film used for IFF1 and IFF2, a FIB-shaped sample was cut and transferred according to §3.2.3. Figure 3.3.7 shows the progression of the tensile test. Note the sample edges appear more irregular than those of the UFS sample (Figure 3.3.4). A great effort was taken to minimize milling times, and the uneven edge is due to differing milling rates of the different areas. Had the milling continued longer, the edges would be smoother. The sample deforms elastically until a crack forms at a triple junction (TJ), shown in Figure 3.3.7b. The crack slowly propagates transgranularly to the right, orthogonal to the loading direction, but is stopped before reaching the edge. A crack initiates at the edge and

59

propagates to the left before the sample fully fails. The left side of the initial crack begins propagating intergranularly, but changes direction and finishes as transgranular propagation. Total elongation was 19% and reduction in width was 23%, demonstrating that in addition to the crack there was quite a bit of plastic deformation elsewhere. Largest grain, one to the right of the TJ, is <110> oriented for a loading direction of <002>.
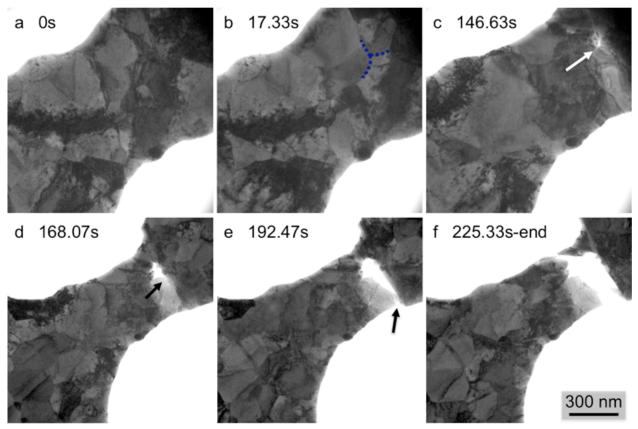
Figure 3.3.7: Still frame images from in-situ TEM tensile test of He[1+] irradiated, FIB-shaped Au thin-film. (a) Initial microstructure. (b) Dashed line overlay of the triple junction where a crack initiates. (c) Crack has initiated (white arrow). (d) The crack has primarily propagated transgranularly (black arrow). (e) Another crack has formed at the sample edge (black arrow). (f) Final microstructure.

3.3.2.5 Discussion

Figure 3.3.8 shows a summary of the mechanical behavior of the four irradiation conditions investigated and Table 3.3.1 summarizes the maximum strain and stress reached by each sample. Irradiation-defect free Au, sample UFF, experiences a sudden 8.3% increase in strain and fails transgranularly; UFS deforms by first initiating a crack at a triple junction and fails transgranularly with a comparatively low total elongation; IFF1 has no visible He[1+] cavities, initiates slip on or near a grain boundary, is highly ductile, and fails transgranularly; IFF2 has visible cavities near, but not in the gage section, and is the only sample to fail intergranularly; the combination of He[1+] irradiation and Ga[3+] ion beam shaping, sample IFS, results in failure initiating at a triple junction after a relatively high total elongation.
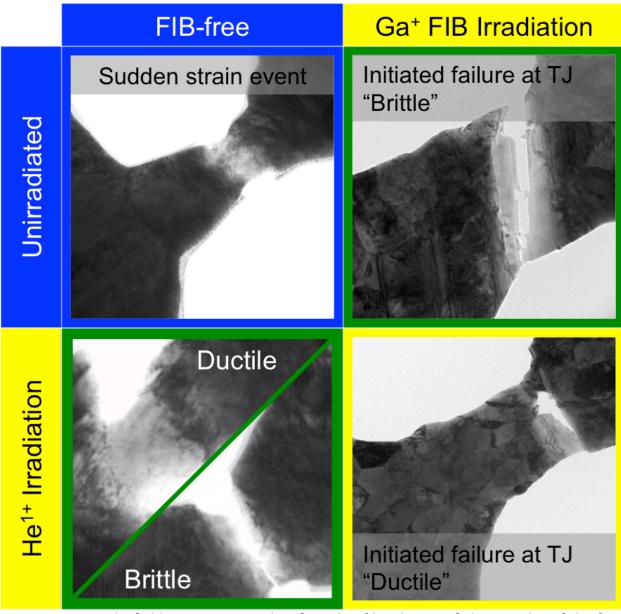
Figure 3.3.8: Bright-field TEM micrographs of Au thin-film showing failure modes of the four irradiation conditions.

Table 3.3.1: Summary of maximum strain and ultimate tensile stress reached for each sample. UTS could not be determined for UFF and IFS.

Sample	UFF	UFS	IFF1	IFF2	IFS
%ε_{max}	27	9.5	>25	1.7	20
UTS (GPa)	NA	0.31	4.33	1.12	NA

It is possible the sudden strain event (8.3%) of UFF is due to the redeposited Au-C surface contamination layer acting as a hardened shell, which causes a sudden strain event once it fails. However, this behavior was not seen in the other two FIB-free samples with similar

contamination layer thicknesses, and the calculated and measured moduli of the other two samples match quite well. If the contamination layer were acting as a hardened shell, the modulus would be higher than expected due to a higher shell modulus and by not including the shell thickness in the CSA measurement. It appears, then, that the contamination layer is not contributing any appreciable effect to the mechanical properties. The surface contamination layer could act as a barrier to dislocation annihilation at the surface, creating a pileup, which could result in a strain burst once overcome. For a strain of 8.3%, a minimum of 250 dislocations must be created in 1/30th second. If a single spiral source is considered, the surface node velocity must be ~6mm/s. Presumably, the UFF sample has fewer initial defects, and as such, the sudden strain event in radiation damage-free films indicates a failure mode that is defect density driven. And indeed, the sample has far fewer defects after the strain burst. To explore this hypothesis the irradiated samples are considered.

30 keV $Ga3^+$ FIB-shaping defects include amorphization, Ga^{3+} implantation, and small defect clusters, but should be localized to ~10 nm of the incident surface[32,34,35]. The UFS stress-strain curve shows similar behavior to in-situ SEM tensile experiments of <100> oriented FIB-shaped Au[148]. Though the SEM experiments show a strength-size dependence, the yield strength is around 300 MPa or below, with failure strains reaching 10-20%. These TEM observations shed some light on the size-effect seen in the SEM study. Cracks were arrested in both FIB-shaped samples at the FIB-damaged edges. It is likely, then, that dislocations are likewise arrested at the edges. For samples fully shaped by the FIB from the bulk, this results in a core-shell structure. Indeed, 3-D DD simulations of FCC pillars have shown that an increased external barrier strength will trap dislocations resulting in an increased flow strength as size decreases[149].

As defect pinning strengths increase, yield strength increases. Irradiation defects such as SFTs, other vacancy clusters, and low-pressure bubbles are sheared by passing dislocations, and can result in the removal of barriers in a channel, localizing slip to this band and decreasing the uniform elongation. As defect pinning strength increases, the Orowan mechanism must take over, leading to cross-slip, double cross-slip, loop creation, etc, increasing work hardening. Both FIB-free irradiated samples show increased strength over UFF and UFS, which is expected for irradiation defects acting as barriers to dislocation motion. However, the remarkable difference in mechanical behavior between the two IFF samples, one failing with the most ductility and the other the least, does not inspire confidence in the present testing scheme, as clearly, crystallographic orientation is a strong factor in these tensile tests.

Only two thing can be said about this set of experiments with any confidence: one, FIB-shaping clearly has some effect at the edge, as initial cracks start at the edges in FIB-free samples, but initial cracks form at triple junctions in FIB-shaped samples, with the edges actually arresting crack propagation; and two, crystallographic orientation plays a large role in determining mechanical behavior at these conditions. These tests include some of the first FIB-free single grain boundary tensile tests and demonstrate the feasibility of investigating grain-boundary effects like embrittlement. However, to effectively study defect mechanisms in thin-films, more control over the initial microstructure, perhaps with bi-crystalline film, is needed.

3.4 Summary and conclusions

The local strain around the helium bubbles is an important parameter in understanding evolving mechanical properties of irradiated materials, but difficult to determine experimentally. Therefore, two novel strain mapping methods, nano-beam diffraction and dark-field inline holography, have been implemented. Nano-beam diffraction strain mapping of a large area at high resolution was carried out using a high frame rate detector. Dark-field inline holography was used to measure the strain field around a bubble at high precision, demonstrating the applicability of this technique to metallic systems with nanoscale defects. Both methods found a peak strain around ~10 nm bubbles of 0.7%, correlating to an internal pressure of 580 MPa, or a vacancy to helium ion ratio of 1V:2.4He. The present work is of general interest for materials design, as it demonstrates how to tailor nanoscale strain fields and measure them with high precision.

Mechanical testing of the same He^{1+} implanted Au thin film did not generate many conclusions when compared to unirradiated and FIB-shaped films, as grain number and orientation results in highly anisotropic behavior at this size scale, obscuring any trends. However, FIB-shaped edges are shown to arrest crack propagation in both unirradiated and irradiated samples, and failure initiates away from these edges, at triple junctions, which is not the case for FIB-free samples. Furthermore, FIB-shaped samples, though ductile, do not exhibit the cup-cone geometry of their FIB-free counterparts. However, crystallographic grain orientations in the film may preclude multiple-slip or single-slip behavior, thereby leading to this observation. It is also interesting the only sample with brittle failure has visible He^{1+} cavities, indicating that helium can indeed embrittle grain boundaries at room temperature. Again, though, crystallographic orientation plays a factor here and cannot be discounted. Thus, further testing with well-defined grain orientations and boundaries is needed before drawing any real conclusions.

4. Conclusion

Presented in this work are in-situ TEM experiments using a picoindenter and digital image correlation to quantitatively measure stress and strain at 15 to 400 frames per second, and dark-field inline holography and nano-beam electron diffraction to map strain in large fields of view. In-situ TEM experiments of a model BCC material, Mo-alloy nano-fibers, show three main results: one, the local true stress around a Frank-Read source activation was measured, with results that compare remarkably well to predicted stress values using the radius of curvature and a large bow-out model; two, the attempt to capture the mechanism responsible for the sudden, large strain bursts seen in dislocation exhausted and starved Mo-alloy nano-fibers using the Gatan K2 camera, show tensile samples fully fail rather than strain soften; and three, the in-situ TEM mechanical tests of unirradiated and He^{1+} and Ni^{2+} irradiated fibers show that collective defect behavior, regardless of type, can lead to similar mechanical properties such as yield strength, ultimate strength, number and size of load drops, and total elongation. In-situ TEM experiments of a model FCC material, Au thin-film, show two main results: one, two novel strain mapping methods, nano-beam diffraction and dark-field inline holography, measure a peak strain of 0.7% in the matrix surrounding ~10 nm bubbles, correlating to an internal bubble pressure of 580 MPa, or a vacancy to helium ion ratio of 1V:2.4He; and two, mechanical testing of the same He^{1+} implanted Au thin film could not generate many conclusions when compared to unirradiated and FIB-shaped films, as grain number and orientation results in highly anisotropic behavior at this size scale, obscuring any trends.

With this thesis, the groundwork for measuring and understanding fundamental defect physics is laid. Immediate future applications of the presented methods include a more detailed analysis, perhaps by using transient strain mapping, of defect interactions, as in the pinning and de-pinning of mobile dislocations by sessile loops in F6 (Figure 2.3.4), which can then be directly compared to current and future defect interaction simulations. Indeed, as mentioned earlier, nano-beam electron diffraction has very recently been applied to in-situ mechanical experiments[126]. Another exciting possible application of strain mapping and in-situ heating or irradiation is the study of the helium bubble to void transition. More long-term experimental hurdles include increasing camera frame rates to study the dislocation multiplication processes that are still too fast to be captured.

The findings of this work demonstrate the reality and feasibility of applying these high-resolution quantitative stress and strain measurement techniques to many in-situ TEM tests. Perhaps the most exciting result presented in this work is that the activation stress of a Frank-Read source can not only be measured with high load and displacement resolution using a commercially available picoindenter and digital image correlation, but that it compares so well to predicted stress values using the dislocation radius of curvature or a simple large bow-out model. This demonstrates that there is no inherent difference between a 300 nm Mo-alloy nano-fiber and a continuum based model. The important implication then, is that small-scale samples can be used to study unit defect interactions without apparent consequence. Additionally, these represent some of the first in-situ TEM tensile experiments of FIB-free single grain boundaries. Results show the sample preparation and testing methods are sound, and with a more controlled microstructure real insights into defect evolution in extreme environments can be gained.

References

[1]   L da Vinci: *I Libri Di Meccanica, reconstructed from the original notes by Arturo Ucelli* (Nendeln, Liechtenstein: Kraus Reprint) (1972).

[2]   WB Parsons: *Engineers and Engineering in the Renaissance* (Cambridge, MA: MIT Press) (1939).

[3]   SS Brenner: Tensile strength of whiskers. *J. Appl. Phys.* **27**, 1484 (1956).

[4]   MD Uchic, DM Dimiduk, JN Florando, and WD Nix: Sample dimensions influence strength and crystal plasticity. *Science (80-.).* **305**, 986 (2004).

[5]   GI Taylor: The Mechanism of Plastic Deformation of Crystals . Part I . Theoretical. *Proc. R. Soc. London. Ser. A* **145**, 362 (1934).

[6]   GI Taylor: The Mechanism of Plastic Deformation of Crystals . Part II . Comparison with Observations. *Proc. R. Soc. London. Ser. A* **145**, 388 (1934).

[7]   E Orowan: Zur Kristallplastizität. I. *Zeitschrift für Phys.* **89**, 605 (1934).

[8]   E Orowan: Zur Kristallplastizität. II. *Zeitschrift für Phys.* **89**, 614 (1934).

[9]   E Orowan: Zur Kristallplastizität. III. *Zeitschrift für Phys.* **89**, 634 (1934).

[10]   M Polanyi: Über eine Art Gitterstörung, die einen Kristall plastisch machen könnte. *Zeitschrift für Phys.* **89**, 660 (1934).

[11]   PB Hirsch, RW Horne, and MJ Whelan: LXVIII. Direct observations of the arrangement and motion of dislocations in aluminium. *Philos. Mag.* **1**, 677 (1956).

[12]   JP Hirth and J Lothe: *Theory of Dislocations* (New York, NY: McGraw-Hill) (1982).

[13]   SP Fitzgerald, S Aubry, SL Dudarev, and W Cai: Dislocation dynamics simulation of Frank-Read sources in anisotropic α-Fe. *Model. Simul. Mater. Sci. Eng.* **20**, 045022 (2012).

[14]   R Groger and V Vitek: Explanation of the discrepancy between the measured and atomistically calculated yield stresses in body-centered cubic metals. *Philos. Mag. Lett.* **87**, 113 (2006).

[15]   JA Hinks: A review of transmission electron microscopes with in situ ion irradiation. *Nucl. Instruments Methods Phys. Res. Sect. B Beam Interact. with Mater. Atoms* **267**, 3652 (2009).

[16]   ML Jenkins, MA Kirk, and WJ Phythian: Experimental studies of cascade phenomena in metals. *J. Nucl. Mater.* **205**, 16 (1993).

[17]   CA English and ML Jenkins: Insight into Cascade Processes Arising from Studies of Cascade Collapse. *Mater. Sci. Forum* **15-18**, 1003 (1987).

[18]   JE Pawel, EE Bloom, LK Mansur, AF Rowcliffe, SJ Zinkle, RE Stoller, and PJ Maziasz: Toward a mechanistic understanding of radiation effects in materials. *Radiat. Eff. Defects Solids* **144**, 287 (1998).

[19]   H Ullmaier: The influence of helium on the bulk properties of fusion reactor structural materials. *Nucl. Fusion* **24**, 1039 (1984).

[20]   LK Mansur: Void swelling in metals and alloys under irradiation: An assessment of the theory. *Nucl. Technol.* **40**, 5 (1978).

[21]   DJ Bacon, YN Osetsky, and D Rodney: Dislocation – Obstacle Interactions at the Atomic Level. *Dislocations in Solids* vol 4859, ed J P Hirth and L P Kubin (2009).

[22]   Y Matsukawa, YN Osetsky, RE Stoller, and SJ Zinkle: Destruction processes of large stacking fault tetrahedra induced by direct interaction with gliding dislocations. *J. Nucl. Mater.* **351**, 285 (2006).

[23]   Z Rong, V Mohles, DJ Bacon, and YN Osetsky: Dislocation dynamics modelling of dislocation – loop interactions in irradiated metals. *Philos. Mag.* **85**, 171 (2005).

[24]   DJ Bacon and YN Osetsky: Modelling dislocation–obstacle interactions in metals exposed to an irradiation environment. *Mater. Sci. Eng. A* **400-401**, 353 (2005).

[25]   Y Matsukawa, YN Osetsky, RE Stoller, and SJ Zinkle: Mechanisms of stacking fault tetrahedra destruction by gliding dislocations in quenched gold. *Philos. Mag.* **88**, 581 (2008).

[26]   YN Osetsky, Y Matsukawa, RE Stoller, and SJ Zinkle: On the features of dislocation–obstacle interaction in thin films: large-scale atomistic simulation. *Philos. Mag. Lett.* **86**, 511 (2006).

[27]   DJ Bacon, YN Osetsky, and Z Rong: Computer simulation of reactions between an edge dislocation and glissile self-interstitial clusters in iron. *Philos. Mag.* **86**, 3921 (2006).

[28]   KE Johanns, A Sedlmayr, P Sudharshan Phani, R Mönig, O Kraft, EP George, and GM Pharr: In-situ tensile testing of single-crystal molybdenum-alloy fibers with various dislocation densities in a scanning electron microscope. *J. Mater. Res.* **27**, 508 (2011).

[29]   S Schmidt, W Sigle, W Gust, and M Ruhle: Gallium segregation at grain boundaries in aluminum. *Zeitschrift für Met.* **93**, 428 (2002).

[30]   E Pereiro-López, W Ludwig, D Bellet, and C Lemaignan: In situ investigation of Al bicrystal embrittlement by liquid Ga using synchrotron imaging. *Acta Mater.* **54**, 4307 (2006).

[31]   H Bei, S Shim, MK Miller, GM Pharr, and EP George: Effects of focused ion beam milling on the nanomechanical behavior of a molybdenum-alloy single crystal. *Appl. Phys. Lett.* **91**, 111915 (2007).

[32]   D Kiener, C Motz, M Rester, M Jenko, and G Dehm: FIB damage of Cu and possible consequences for miniaturized mechanical tests. *Mater. Sci. Eng. A* **459**, 262 (2007).

[33]   S Reyntjens and R Puers: A review of focused ion beam applications in microsystem technology. *J. Micromechanics Microengineering* **11**, 287 (2001).

[34]   CA Volkert and AM Minor: Focused Ion Beam Microscopy and Micromachining. *MRS Bull.* **32**, 389 (2007).

[35]   J Mayer, LA Giannuzzi, T Kamino, and J Michael: TEM Sample Preparation and FIB-Induced Damage. *MRS Bull.* **32**, 400 (2007).

[36]   S Bals, W Tirry, R Geurts, Z Yang, and D Schryvers: High-Quality Sample Preparation by Low kV FIB Thinning for Analytical TEM Measurements. *Microsc. Microanal.* **13**, 80 (2007).

[37]   MB Lowry, D Kiener, MM LeBlanc, C Chisholm, JN Florando, J Morris, J W, and AM Minor: Achieving the ideal strength in annealed molybdenum nanopillars. *Acta Mater.* **58**, 5160 (2010).

[38]   KY Xie, S Shrestha, Y Cao, PJ Felfer, Y Wang, X Liao, JM Cairney, and SP Ringer: The effect of pre-existing defects on the strength and deformation behavior of α-Fe nanopillars. *Acta Mater.* **61**, 439 (2013).

[39]   ZW Shan, RK Mishra, SA Syed Asif, OL Warren, and AM Minor: Mechanical annealing and source-limited deformation in submicrometre-diameter Ni crystals. *Nat. Mater.* **7**, 115 (2008).

[40]   M Legros: In situ mechanical TEM: Seeing and measuring under stress with electrons. *Comptes Rendus Phys.* **15**, 224 (2014).

[41]   HD Espinosa, RA Bernal, and T Filleter: In-Situ TEM Electromechanical Testing of Nanowires and Nanotubes. *Small* **8**, 3233 (2012).

[42]   HGF Wilsdorf: Apparatus for the Deformation of Foils in an Electron Microscope. *Rev. Sci. Instrum.* **29**, 323 (1958).

[43]   Y Zhu, A Corigliano, and HD Espinosa: A thermal actuator for nanoscale in-situ microscopy testing: design and characterization. *J. Micromechanics Microengineering* **16**, 242 (2006).

[44]   MA Haque and MTA Saif: In-situ Tensile Testing of Nano-scale Specimens in SEM and TEM. *Exp. Mech.* **42**, 123 (2002).

[45]   MJ Hÿtch and AM Minor: Observing and measuring strain in nanostructures and devices with transmission electron microscopy. *MRS Bull.* **39**, 138 (2014).

[46]   A Béché, JL Rouvière, JP Barnes, and D Cooper: Strain measurement at the nanoscale: Comparison between convergent beam electron diffraction, nano-beam electron diffraction, high resolution imaging and dark field electron holography. *Ultramicroscopy* **131**, 10 (2013).

[47]   JM Cowley: Twenty forms of electron holography. *Ultramicroscopy* **41**, 335 (1992).

[48]   H Guo, K Chen, Y Oh, K Wang, C Dejoie, SA Syed Asif, OL Warren, ZW Shan, J Wu, and a M Minor: Mechanics and Dynamics of the Strain-Induced M1-M2 Structural Phase Transition in Individual VO(2) Nanowires. *Nano Lett.* **11**, 3207 (2011).

[49]   C Chisholm, H Bei, MB Lowry, J Oh, SA Syed Asif, OL Warren, ZW Shan, EP George, and AM Minor: Dislocation starvation and exhaustion hardening in Mo alloy nanofibers. *Acta Mater.* **60**, 2258 (2012).

[50]   I Chasiotis and WG Knauss: A new microtensile tester for the study of MEMS materials with the aid of atomic force microscopy. *Exp. Mech.* **42**, 51 (2002).

[51]   KJ Hemker and WN Sharpe: Microscale Characterization of Mechanical Properties. *Annu. Rev. Mater. Res.* **37**, 93 (2007).

[52]   WC Oliver and JB Pethica: Patent US4848141A– Method for continuous determination of the elastic stiffness of contact between two bodies. (1989).

[53]   Y Zhu and HD Espinosa: An electromechanical material testing system for in situ electron microscopy and applications. *Proc. Natl. Acad. Sci. U. S. A.* **102**, 14503 (2005).

[54]   H Bei, S Shim, GM Pharr, and EP George: Effects of pre-strain on the compressive stress–strain response of Mo-alloy single-crystal micropillars. *Acta Mater.* **56**, 4762 (2008).

[55] HS Park, W Cai, and HD Espinosa: Mechanics of Crystalline Nanowires. *MRS Bull.* **34**, (2009).

[56] WW Gerberich, J Michler, WM Mook, R Ghisleni, F Ostlund, DD Stauffer, and R Ballarini: Scale effects for strength, ductility, and toughness in "brittle" materials. *J. Mater. Res.* **24**, (2009).

[57] JR Greer and JTM De Hosson: Plasticity in small-sized metallic systems: Intrinsic versus extrinsic size effect. *Prog. Mater. Sci.* **56**, 654 (2011).

[58] DS Gianola and C Eberl: Micro- and Nanoscale Testing of Materials. *Journal of Materials* vol 61 pp 24–35 (2009).

[59] GM Pharr, EG Herbert, and YF Gao: The Indentation Size Effect: A Critical Examination of Experimental Observations and Mechanistic Interpretations. *Annu. Rev. Mater. Res.* **40**, 271 (2010).

[60] MD Uchic, PA Shade, and DM Dimiduk: Plasticity of Micrometer-Scale Single Crystals in Compression. *Annu. Rev. Mater. Res.* **39**, 361 (2009).

[61] JA El-Awady: Unravelling the physics of size-dependent dislocation-mediated plasticity. *Nat. Commun.* **6**, 1 (2015).

[62] H Ikehata, N Nagasako, S Kuramoto, and T Saito: Designing New Structural Materials Using Density Functional Theory: The Example of Gum Metal. *MRS Bull.* **31**, 688 (2006).

[63] M Hara, Y Shimizu, T Yano, N Takesue, T Furuta, and S Kuramoto: Mechanical anisotropy and ideal strength in a multifunctional Ti-Nb-Ta-Zr-O alloy (Gum Metal). *Int. J. Mater. Res.* **100**, 345 (2009).

[64] SJ Zinkle and GS Was: Materials challenges in nuclear energy. *Acta Mater.* **61**, 735 (2013).

[65] H Bei and EP George: Microstructures and mechanical properties of a directionally solidified NiAl–Mo eutectic alloy. *Acta Mater.* **53**, 69 (2005).

[66] PS Phani, KE Johanns, G Duscher, A Gali, EP George, and GM Pharr: Scanning transmission electron microscope observations of defects in as-grown and pre-strained Mo alloy fibers. *Acta Mater.* **59**, 2172 (2011).

[67] E Oveisi, B Bártová, S Gerstl, J Zimmermann, C Marichal, H Van Swygenhoven, and C Hébert: Nanoprecipitates in single-crystal molybdenum-alloy nanopillars detected by TEM and atom probe tomography. *Scr. Mater.* **69**, 41 (2013).

[68] RK Ham: The determination of dislocation densities in thin films. *Philos. Mag.* **6**, 1183 (1961).

[69] J Kwon, ML Bowers, MC Brandes, V Mccreary, IM Robertson, PS Phani, H Bei, YF Gao, GM Pharr, EP George, and MJ Mills: Characterization of dislocation structures and deformation mechanisms in as-grown and deformed directionally solidified NiAl–Mo composites. *Acta Mater.* **89**, 315 (2015).

[70] K Hattar, DC Bufford, and DL Buller: Concurrent in situ ion irradiation transmission electron microscope. *Nucl. Instruments Methods Phys. Res. B* **338**, 56 (2014).

[71] JF Ziegler, MD Ziegler, and JP Biersack: SRIM - The stopping and range of ions in matter (2010). *Nucl. Instruments Methods Phys. Res. B* **268**, 1818 (2010).

[72] M Li, MA Kirk, PM Baldo, D Xu, and BD Wirth: Study of defect evolution by TEM with in situ ion irradiation and coordinated modeling. *Philos. Mag.* **92**, 2048 (2012).

[73] DJ Mazey, BL Eyre, JH Evans, SK Erents, and GM McCracken: A transmission electron microscopy study of molybdenum irradiated with helium ions. *J. Nucl. Mater.* **64**, 145 (1977).

[74] P Rao and G Thomas: Defects in neutron irradiated molybdenum. *Acta Metall.* **15**, 1153 (1967).

[75] ME Downey and BL Eyre: Neutron irradiation damage in molybdenum. *Philos. Mag.* **11**, 53 (1965).

[76] CA English, BL Eyre, AF Bartlett, and HNG Wadley: The influence of material purity and irradiation temperature on self-ion damage in molybdenum. *Philos. Mag.* **35**, 533 (1977).

[77] AP Selby, D Xu, N Juslin, NA Capps, and BD Wirth: Primary defect production by high energy displacement cascades in molybdenum. *J. Nucl. Mater.* **437**, 19 (2013).

[78] M Eldrup, M Li, LL Snead, and SJ Zinkle: Characterization of defect accumulation in neutron-irradiated Mo by positron annihilation spectroscopy. *Nucl. Instruments Methods Phys. Res. B* **266**, 3602 (2008).

[79] SJ Zinkle: Radiation-Induced Effects on Microstructure. *Comprehensive Nuclear Materials* vol 1, ed R J M Konings (Amsterdam: Elsevier Inc.) pp 65–98 (2012).

[80] ML Jenkins: Characterisation of radiation-damage microstructures by TEM. *J. Nucl. Mater.* **216**, 124 (1994).

[81]   H Bei, S Shim, EP George, MK Miller, EG Herbert, and GM Pharr: Compressive strengths of molybdenum alloy micro-pillars prepared using a new technique. *Scr. Mater.* **57**, 397 (2007).

[82]   C Eberl, R Thompson, D Gianola, and S Bundschuh: Digital Image Correlation and Tracking with Matlab. (2006).

[83]   J Marian, W Cai, and V V Bulatov: Dynamic transitions from smooth to rough to twinning in dislocation motion. *Nat. Mater.* **3**, 158 (2004).

[84]   W Cai, V V Bulatov, JF Justo, AS Argon, and S Yip: Kinetic Monte Carlo approach to modeling dislocation mobility. *Comput. Mater. Sci.* **23**, 124 (2002).

[85]   MS Duesbery and V Vitek: Plastic Anisotropy in BCC Transition Metals. *Acta Mater.* **46**, 1481 (1998).

[86]   SI Rao, DM Dimiduk, M Tang, MD Uchic, TA Parthasarathy, and C Woodward: Estimating the strength of single-ended dislocation sources in micron-sized single crystals. *Philos. Mag.* **87**, 4777 (2007).

[87]   CR Weinberger and W Cai: Surface-controlled dislocation multiplication in metal micropillars. *Proc. Natl. Acad. Sci. U. S. A.* **105**, 14304 (2008).

[88]   CR Weinberger: Dislocation drag at the nanoscale. *Acta Mater.* **58**, 6535 (2010).

[89]   W Cai, V V Bulatov, S Yip, and AS Argon: Kinetic Monte Carlo modeling of dislocation motion in BCC metals. *Mater. Sci. Eng. A* **310**, 270 (2001).

[90]   AK Seeger and L Hollang: The flow-stress asymmetry of ultra-pure molybdenum single crystals. *Mater. Trans.* **41**, 141 (2000).

[91]   L Hollang, D Brunner, and A Seeger: Work hardening and flow stress of ultrapure molybdenum single crystals. *Mater. Sci. Eng. A* **319-321**, 233 (2001).

[92]   A Portevin and F le Chatelier: Tensile tests of alloys undergoing transformation. *C. R. Hebd. Seances Acad. Sci.* **176**, 507 (1923).

[93]   T Böhlke, G Bondár, Y Estrin, and MA Lebyodkin: Geometrically non-linear modeling of the Portevin-Le Chatelier effect. *Comput. Mater. Sci.* **44**, 1076 (2009).

[94]   MS Bharathi, S Rajesh, and G Ananthakrishna: A dynamical model for the Portevin-Le Chatelier bands. *Scr. Mater.* **48**, 1355 (2003).

[95]   S Li, X Ding, J Deng, T Lookman, J Li, X Ren, J Sun, and A Saxena: Superelasticity in bcc nanowires by a reversible twinning mechanism. *Phys. Rev. B* **82**, 1 (2010).

[96]   SJ Wang, H Wang, K Du, W Zhang, ML Sui, and SX Mao: Deformation-induced structural transition in body-centred cubic molybdenum. *Nat. Commun.* **5**, 1 (2014).

[97]   T LaGrange, MR Armstrong, K Boyden, CG Brown, GH Campbell, JD Colvin, WJ DeHope, AM Frank, DJ Gibson, F V Hartemann, JS Kim, WE King, BJ Pyke, BW Reed, MD Shirk, RM Shuttlesworth, BC Stuart, BR Torralva, and ND Browning: Single-shot dynamic transmission electron microscopy. *Appl. Phys. Lett.* **89**, 044105 (2006).

[98]   H Bei, YF Gao, S Shim, EP George, and GM Pharr: Strength differences arising from homogeneous versus heterogeneous dislocation nucleation. *Phys. Rev. B* **77**, 060103 (1 (2008).

[99]   PE Loya, YZ Xia, C Peng, H Bei, P Zhang, J Zhang, EP George, J Lou, YF Gao, and J Lou: Yield strength dependence on strain rate of molybdenum-alloy nanofibers. *Appl. Phys. Lett.* **104**, 1 (2014).

[100] H Matsui and H Kimura: Dislocation configurations and work hardening in molybdenum single crystals deformed in tension at 77 and 293K. *Trans. Japan Inst. Met.* **22**, 481 (1981).

[101] L Huang, Q-J Li, Z-W Shan, J Li, J Sun, and E Ma: A new regime for mechanical annealing and strong sample-size strengthening in body centred cubic molybdenum. *Nat. Commun.* **2**, 1 (2011).

[102] M Li, M Eldrup, TS Byun, N Hashimoto, LL Snead, and SJ Zinkle: Low temperature neutron irradiation effects on microstructure and tensile properties of molybdenum. *J. Nucl. Mater.* **376**, 11 (2008).

[103] DF Nelson: Second and Higher Order Elastic Constants. *Landolt-Börnstein - Numerical Data and Functional Relationships in Science and Technology* vol 29a (1992).

[104] JF Nye: *Physical Properties of Crystals: Their Representation by Tensors and Matrices* (Clarendon Press) (1985).

[105] HB Huntington: The elastic constants of crystals. *Solid State Phys.* **7**, 213 (1958).

[106] RFS Hearmon: The Elastic Constants of Anisotropic Materials. *Rev. Mod. Phys.* **18**, 409 (1946).

[107] RFS Hearmon: Temperature dependence of the elastic constants of aluminum. *Solid State Commun.* **37**, 915 (1981).

[108] HPR Frederikse: Elastic Constants of Single Crystals. *CRC Handbook of Chemistry and Physics* ed W M Haynes pp 12:35–12:40

[109] RM Bozorth, WP Mason, and HJ McSkimin: Frequency Dependence of Elastic Constants and Losses in Nickel. *Bell Syst. Tech. J.* **30**, 970 (1951).

[110] FH Featherston and JR Neighbours: Elastic Constants of Tantalum, Tungsten, and Molybdenum. *Phys. Rev.* **130**, 1324 (1963).

[111] DI Bolef and J De Klerk: Elastic Constants of Single-Crystal Mo and W between 77 and 500K. *J. Appl. Phys.* **33**, 2311 (1962).

[112] JM Dickinson and PE Armstrong: Temperature Dependence of the Elastic Constants of Molybdenum. *J. Appl. Phys.* **38**, 602 (1967).

[113] DL Davidson and FR Brotzen: Elastic Constants of Molybdenum-Rich Rhenium Alloys in the Temperature Range −190°C to +100°C. *J. Appl. Phys.* **39**, 5768 (1968).

[114] D Kiener and AM Minor: Source Truncation and Exhaustion: Insights from Quantitative in situ TEM Tensile Testing. *Nano Lett.* **11**, 3816 (2011).

[115] KF Murphy, LY Chen, and DS Gianola: Effect of organometallic clamp properties on the apparent diversity of tensile response of nanowires. *Nanotechnology* **24**, 1 (2013).

[116] Z Ma, H Zhao, H Cheng, and J Li: Effects of 2D misalignment on tensile results and corresponding correction methods to obtain the true stress–strain curve. *Meas. Sci. Technol.* **25**, 115011 (1 (2014).

[117] R Agrawal, B Peng, EE Gdoutos, and HD Espinosa: Elasticity size effects in ZnO nanowires-a combined experimental-computational approach. *Nano Lett.* **8**, 3668 (2008).

[118] ET Lilleodden: *Indentation-Induced Plasticity of Thin Metals Films* (Stanford University) (2001).

[119] SJ Zinkle: Microstructures and mechanical properties of irradiated metals and alloys. *Proceedings of the NATO Advanced Study Institute on Materials Issues for Generation IV Systems: Status, Open Questions and Challenges* pp 227–44 (2008).

[120] SJ Zinkle and NM Ghoniem: Operating temperature windows for fusion reactor structural materials. *Fusion Eng. Des.* **51-52**, 55 (2000).

[121] PR Rios, F Siciliano Jr, HRZ Sandim, RL Plaut, and AF Padilha: Nucleation and growth during recrystallization. *Mater. Res.* **8**, 225 (2005).

[122] J Akella, SN Vaidya, and GC Kennedy: Melting of sodium chloride at pressure to 65 kbar. *Phys. Rev.* **185**, 1135 (1969).

[123] C Chisholm, C Gammer, VB Özdöl, K Hattar, P Hosemann, DC Chrzan, and AM Minor: *Nano-scale strain mapping of helium bubbles in gold, in preparation* (2015).

[124] T Latychevskaia, P Formanek, CT Koch, and A Lubk: Off-axis and inline electron holography: Experimental comparison. *Ultramicroscopy* **110**, 472 (2010).

[125] CT Koch, VB Özdöl, and PA van Aken: An efficient, simple, and precise way to map strain with nanometer resolution in semiconductor devices. *Appl. Phys. Lett.* **96**, 091901 1 (2010).

[126] C Gammer, J Kacher, J Ciston, C Czarnik, OL Warren, and AM Minor: Local and transient nanoscale strain mapping during in-situ deformation, in preparation.

[127] M Hÿtch, F Houdellier, F Hüe, and E Snoeck: Nanoscale holographic interferometry for strain measurements in electronic devices. *Nature* **453**, 1086 (2008).

[128] R Bierwolf, M Hohenstein, F Phillipp, O Brandt, GE Crook, and K Ploog: Direct measurement of local lattice distortions in strained layer structures by HREM. *Ultramicroscopy* **49**, 273 (1993).

[129] MJ Hÿtch, E Snoeck, and R Kilaas: Quantitative measurement of displacement and strain fields from HREM micrographs. *Ultramicroscopy* **74**, 131 (1998).

[130] YY Wang, J Bruley, H van Meer, J Li, A Domenicucci, CE Murray, and J Rouviere: Strain mapping of Si devices with stress memorization processing. *Appl. Phys. Lett.* **103**, 052104 1 (2013).

[131] F Hüe, M Hÿtch, F Houdellier, H Bender, and A Claverie: Strain mapping of tensiley strained silicon transistors with embedded Si[sub 1−y]C[sub y] source and drain by dark-field holography. *Appl. Phys. Lett.* **95**, 073103 (2009).

[132] CT Koch: A flux-preserving non-linear inline holography reconstruction algorithm for partially coherent electrons. *Ultramicroscopy* **108**, 141 (2008).

[133] C Gammer: Developed by.

[134] GE Lucas: The evolution of mechanical property change in irradiated austenitic stainless steels. *J. Nucl. Mater.* **206**, 287 (1993).

[135] R Schäublin, J Henry, and Y Dai: Helium and point defect accumulation: (i) microstructure and mechanical behaviour. *Comptes Rendus Phys.* **9**, 389 (2008).

[136] NM Ghoniem, S Sharafat, JM Williams, and LK Mansur: Theory of helium transport and clustering in materials under irradiation. *J. Nucl. Mater.* **117**, 96 (1983).

[137] SE Donnelly: The density and pressure of helium in bubbles in implanted metals: A critical review. *Radiat. Eff.* **90**, 1 (1985).

[138] CA Walsh, J Yuan, and LM Brown: A procedure for measuring the helium density and pressure in nanometre-sized bubbles in irradiated materials using electron-energy-loss spectroscopy. *Philos. Mag. A* **80**, 1507 (2000).

[139] S Fréchard, M Walls, M Kociak, JP Chevalier, J Henry, and D Gorse: Study by EELS of helium bubbles in a martensitic steel. *J. Nucl. Mater.* **393**, 102 (2009).

[140] SE Donnelly, AA Lucas, and JP Vigneron: The density of helium in bubbles in implanted materials: Results from VUV absorption and EEL spectroscopy. *Radiat. Eff.* **78**, 337 (1983).

[141] W Jager, R Manzke, G Crecelius, H Trinkaus, R Zeller, J Fink, and HL Bay: Density and pressure of helium in small bubbles in metals. *J. Nucl. Mater.* **111 & 112**, 674 (1982).

[142] Y Wu, RG Odette, T Yamamoto, J Ciston, and P Hosemann: An electron eneregy loss spectroscopy study of helium bubbles in nanostructured ferritic alloys. *Fusion React. Mater. Progr.* **54**, 173 (2013).

[143] W Thomson: On the Equilibrium of Vapour at a Curved Surface of Liquid. *Philos. Mag. Ser. 4* **42**, 448 (1871).

[144] A Caro, D Schwen, J Hetherly, and E Martinez: The capillarity equation at the nanoscale: Gas bubbles in metals. *Acta Mater.* **89**, 14 (2015).

[145] H Trinkaus and BN Singh: Helium accumulation in metals during irradiation – where do we stand? *J. Nucl. Mater.* **323**, 229 (2003).

[146] P Mohazzabi: Temperature dependence of the elastic constants of copper, gold and silver. *J. Phys. Chem. Solids* **46**, 147 (1985).

[147] SM Collard: *High-temperature elastic constants of gold single-crystals* (Rice University) (1991).

[148] J-Y Kim and JR Greer: Tensile and compressive behavior of gold and molybdenum single crystals at the nano-scale. *Acta Mater.* **57**, 5245 (2009).

[149] JA El-Awady, SI Rao, C Woodward, DM Dimiduk, and MD Uchic: Trapping and escape of dislocations in micro-crystals with external and internal barriers. *Int. J. Plast.* **27**, 372 (2011).